Evaluating SIR in 3D mmWave Deployments: Direct Modeling and Feasible Approximations

Roman Kovalchukov, Dmitri Moltchanov, Andrey Samuylov, Aleksandr Ometov, *Member, IEEE*, Sergey Andreev, *Senior Member, IEEE*, Yevgeni Koucheryavy, *Senior Member, IEEE*, and Konstantin Samouylov

Recently, new opportunities for utilizing the extremely high frequencies have become instrumental to design the fifth-generation (5G) mobile technology. The use of highly directional antennas in millimeter-wave (mmWave) bands poses an important question of whether 2D modeling suffices to capture the resulting system performance accurately. In this work, we develop a novel mathematical framework for performance assessment of the emerging 3D mmWave communication scenarios, which takes into account vertical and planar directivities at both ends of a radio link, blockage effects in three dimensions, and random heights of communicating entities. We also formulate models having different levels of details and verify their accuracy for a wide range of system parameters. We show that capturing the randomness of both Tx and Rx heights as well as the vertical antenna directivities becomes crucial for accurate system characterization. The conventional planar models provide overly optimistic results that overestimate performance. For instance, the model with fixed heights that disregards the effect of vertical exposure is utterly pessimistic. Other two models, one having random heights and neglecting vertical exposure and another one characterized by fixed heights and capturing vertical exposure are less computationally expensive and can be used as feasible approximations for certain ranges of input parameters.

***Index Terms*—Interference, mmWave systems, SIR, 3D modeling, directional antennas, blockage, 5G**

I. Introduction

With the adoption of advanced communication technology in the forthcoming 5G networks [1], the wireless community envisions that multiple handheld and wearable devices are to be placed on and around user bodies [2]. These capable 'carriables' and 'wearables' may need to cooperate in proximity while utilizing the emerging millimeter-wave (mmWave) radios in ultra-dense deployments (e.g., augmented reality glasses in crowded scenarios). The use of mmWave technology allows for enabling extremely high network capacity and achieving lower latency as compared to the conventional communication under 6GHz [3]. As a result, mmWave systems are expected to soon become an integral part of 5G mobile networks by supporting unprecedented data rates at the air interface along with more efficient spatial frequency reuse.

R. Kovalchukov, D. Moltchanov, A. Samuylov, A. Ometov, S. Andreev, and Y. Koucheryavy are with Tampere University, Finland. Emails: {roman.kovalchukov, dmitri.moltchanov, sergey.andreev, evgeni.koucheryavy}@tut.fi

K. Samouylov is with RUDN University, Moscow, Russia. Email: ksam@sci.pfu.edu.ru

The publication was supported by the Ministry of Education and Science of the Russian Federation (project No. 2.882.2017/4.6).

Correspondence: dmitri.moltchanov@tut.fi

To this aim, the utilization of mmWave bands, such as 28, 60, and 72GHz, has recently gained attention [4]. The higher free-space propagation loss at these frequencies can be partially compensated by the use of highly directional antenna radiation patterns at both the transmitting and the receiving ends of a link. The resultant 'pencil' beams are expected to reduce the interfering signals; hence, improving performance under specific conditions while approaching the noise-limited communication regime [5]. Another feature connected with the mmWave band is the incapability of the electromagnetic waves at these frequencies to 'travel around' the objects, whose size is larger than several centimeters. Therefore, various objects in the radio channel, such as human bodies, lampposts, and buildings, act as blockers to a propagating wave [6].

The evolution of communication systems in the 5G era is accompanied by the increasing complexity of the considered use cases. The envisioned use of drones to deliver service to massive crowds on the move as well as widespread utilization of 'high-end' wearable electronics (e.g., augmented reality glasses) will enable wireless connectivity in three dimensions [7]. Similarly, the emerging ultra-dense 5G scenarios, such as shopping mall deployments [8], embrace another powerful paradigm of device-to-device (D2D) communication, which is expected to push the limits of (beyond-)5G wireless systems by also exploring the third dimension, since the heights of communicating entities may become random.

In this work, we consider these emerging 3D mmWave communication scenarios with directional antennas at both transmitting (Tx) and receiving (Rx) ends of a link, having random heights and positions of the communicating entities, as well as possible blockage of radio propagation paths. Extending the tools of planar stochastic geometry to the third dimension, we derive novel expressions for the mean interference and signal-to-interference ratio (SIR). After obtaining these metrics, we continue with a numerical study to reveal the crucial effects pertaining to 3D mmWave communication scenarios as well as assess the accuracy of several simplified models that are the special cases of our developed more complex solution.

The main contributions of this work are as follows:

- novel mathematical framework allowing to capture the effects of random heights of communicating entities, planar and vertical directionalities of Tx and Rx antennas, as well as 3D blockage phenomenon for interference and SIR analysis in 3D mmWave scenarios;
- rigorous performance evaluation regarding the effects of

various system parameters, which shows that (i) randomness of Tx and Rx heights and vertical exposure probability are critical for accurate performance assessment of 3D mmWave deployments; (ii) the conventional planar model may provide optimistic results that overestimate the mean SIR by as much as 20dB; (iii) the model with fixed heights that disregards the effect of vertical directivity is utterly pessimistic, and the gap between these two extremes may approach $40 - 60$dB; (iv) there exist simpler models that provide accurate approximations for the limited ranges of system parameters;

• performance assessment of various mmWave communication scenarios, including terrestrial, drone-aided, and D2D deployments, which indicates that for the same intensity of communicating entities the drone-assisted deployments are characterized by the best SIR conditions slightly outperforming the standard ground mmWave deployments and having dramatic gains over the D2D case.

The rest of the paper is organized as follows. Section II reviews the related work. The system model is formulated in Section III. The analysis is conducted in Section IV. Subsection IV-C outlines the special cases of the proposed model. Numerical assessment of the model and the examples that address various communication scenarios are provided in Section V. Conclusions are drawn in the last section.

II. Related Work

Conventionally, the performance of cellular communication systems has been assessed with the tools of *planar* stochastic geometry [9]. In that framework, the communicating entities are represented as a realization of a spatial process on the plane, while the metrics of interest are expressed as functions of the Euclidean distance between them. Since the heights of the communicating devices – both the user equipment (UE) and the base station (BS) – are relatively small as compared to the coverage range of a radio link, the distance between the two nodes can be assumed to be planar, and thus geometric methods can be applied to capture the key performance metrics reasonably well, which includes interference, SIR, and channel capacity.

Despite the increased use of highly directional antenna radiation patterns, random heights of the involved entities, and the emergence of complex 3D blockage situations, the tools of planar stochastic geometry remain the most commonly employed for the performance analysis of mmWave systems. The moments of interference and SIR for mmWave systems in the presence of blockage have been derived in [10], [11]. The Laplace transform (LT) of interference and SIR probability density functions (pdfs) in the absence of blockage have been produced in [12]. The LT of SIR for the mmWave system operating at 28GHz has been reported in [13], [14].

In [15], the authors provide SIR approximations for mmWave and terahertz systems in the presence of atmospheric absorption. More recently, engineering studies that address various implementation aspects of mmWave networks started to proliferate, see, e.g., [16], [17], [18]. However, all of the referred studies assume 2D planar deployments, which may lead to significant overestimation of the actual interference in mmWave deployments, thus affecting the SIR and capacity estimates.

Over the last two decades, several authors questioned the popular 2D approximations of real-world 3D cellular network deployments. The work in [19] from the early 90s focused the community's attention on the challenge of 3D antenna analysis with respect to the signal incident angles. Particularly, the authors demonstrated that the use of 3D modeling allows to isolate the null appearances in the antenna radiation pattern more accurately as compared to the 2D approach. A decade later, the study in [20] rattled the 2D approximation conventionally employed in wireless network planning with several illustrative examples, where it leads to significant deviations from the optimal design.

Notably, the 'manifest' was such that the network planners, algorithm designers, and policy makers rely on a small set of radio propagation scenarios, by often assuming fixed Rx antenna heights. Therefore, the network design might be heavily affected by the 2D approximation at hand and more advanced 3D models are required for accurate modeling, development, and planning of the emerging radio systems. Specifically, the differences in the signal-to-interference-plus-noise ratio (SINR) of up to 20dB have been revealed in several scenarios. Similar ideas have been propagated in [21], [22].

The recent push for taming higher frequency bands, where larger bandwidths for 5G mmWave systems are becoming available, revives the discussion about the need for 3D models. Today, most of the studies in this area are related to simulations and measurements conducted in 3D where the focus is set on mmWave communications. For example, [23] focuses on developing a 3D model of the body blockage for smart wearable devices in indoor square premises. Indeed, the use of highly directional antennas, limited coverage range of the mmWave access points (APs), as well as a broader range of communication scenarios may inherently require capturing the third dimension. The authors of [24] elaborate on the analytical model for a 3D massive MIMO system that supports the elevation dimension and thus improves the system SINR.

Further, [25] considers a more realistic "3D+" case, where the APs are located higher than the UEs. One of the latest works in [26] describes the 3D fluid model, which allows to evaluate the cumulative distribution function (CDF) of SINR. The authors demonstrate that their proposed model provides higher accuracy than the counterpart 2D model when compared with simulations. Overall, many works are attempting to evaluate mmWave in 3D, but most of them rely on ray-based modeling techniques that are computationally hungry [27], [28], [29], [30]. One of the reasons to develop an analytical model is to reduce the time required for system-level network evaluation.

In our study [31], we preliminarily examined mmWave deployments with random heights of the communicating Tx nodes having highly directional radiation patterns as well as omnidirectional Rx nodes. Even though the corresponding analysis becomes much more complicated in contrast to 2D modeling, the produced numerical results indicate that the error of approximation for SIR heavily depends on the antenna directivity pattern and may reach as high as 40dB. Such error

levels may not be neglected as they can lead to extremely sub-optimal network deployment and system design decisions.

III. System Model

In this section, we formalize our system model by specifying the 3D deployment, the antenna radiation pattern, as well as the propagation and blockage models. We also introduce the target metrics of interest. Notation used in this paper is summarized in Table I.

A. Network Deployment and Blockage Model

The considered deployment model is illustrated in Fig. 1(a). Assume that the locations of Rx nodes, labeled as R_i, $i = 0, 1, \ldots$, are modeled by a Poisson point process in $\Re^2$ with the intensity of λ. Each Rx is associated with a Tx labeled as T_i. Positions of the Tx nodes are distributed uniformly within the circle of radius R_T centered at the Rx. The Tx nodes are assumed to use the same frequency channel, thereby acting as 'interferers' to the tagged Rx. The heights of Tx and Rx nodes, H_T and H_R, follow an exponential distribution with the parameters μ_T and μ_R, respectively. Hence, the UE may be located not only in the user's hand but anywhere on the body. Rx and Tx nodes are associated with the communicating entities, e.g., humans are represented as cylinders with the radius of r_B, while the height, H_B, follows an exponential distribution with the parameter μ_B.

Among the Tx-Rx pairs, we randomly select an arbitrary one (R_0, T_0) and limit the effective interference area around the tagged Rx by a circle of radius R_I. The interference created by the Tx nodes located outside is assumed to be negligible, i.e., lower than the noise floor. R_I is computed as a function of the propagation model, transmit power, and antenna directivity. In Fig. 1(a), the green bars represent the communicating pair of interest, while other bars correspond to competing entities, whose transmission may or may not affect the tagged Rx. Note that our model also considers the scenario where the radiation passes over the 'heads' of the blockers. However, as this work primarily focuses on the three-dimensional effects of blockage, the self-blockage phenomenon is not included.

We further assume that the communicating entities may occlude the line-of-sight (LoS) path between the interferers and the tagged Rx. Interference from a specific Tx may reach the tagged Rx only if its transmission is directed towards the tagged Rx and the LoS path is not blocked. In Fig. 1(a), the red bars represent the interfering pair affecting the tagged Rx, while the blue bars correspond to the pair, whose transmission is blocked. One may further extend this model by assuming an additional external Poisson field of blockers.

B. Propagation and Antenna Models

In this study, the power at the receiver is modeled by following $P_R(r) = Ar^{-\zeta}$ [32], where ζ is the loss exponent, A is the factor accounting for the transmit power, frequency, and antenna gains, and r is the propagation distance. We consider that the radiation patterns of the transmitting and receiving antennas have similar shapes with different vertical and planar directivities. An antenna pattern is approximated as a pyramidal zone with the vertical and planar angles, $\alpha_{T,V}$ and $\alpha_{T,H}$, respectively, as displayed in Fig. 1(b).

To determine the gain A corresponding to certain directivities (α_V, α_H), observe that the surface area of the wavefront equals the area of the spherical rectangle shown in Fig. 1(b). Using the spherical law of cosines [33], we express $\cos\chi$ as

$$\begin{aligned}\cos\chi &= \frac{\cos\left(\frac{\pi}{2}-\frac{L_H}{2}\right)-\cos\left(\frac{\pi}{2}-\frac{L_H}{2}\right)\cos\left(L_V\right)}{\sin\left(\frac{\pi}{2}-\frac{L_H}{2}\right)\sin\left(L_V\right)} = \\ &= \frac{\sin\left(\frac{L_H}{2}\right)}{cos\left(\frac{L_H}{2}\right)}\frac{1-\cos\left(L_V\right)}{\sin\left(L_V\right)} = \\ &= \tan\left(\frac{L_H}{2}\right)\tan\left(\frac{L_V}{2}\right). \end{aligned} \tag{1}$$

Observe that one quarter of the spherical excess of the rectangle in Fig. 1(b) is $(\rho - \pi/2)$, which implies

$$\cos\left(\rho-\frac{\pi}{2}\right) = \tan\left(\frac{L_H}{2}\right)\tan\left(\frac{L_V}{2}\right), \tag{2}$$

where L_H and L_V are spherical geodesics.

The spherical geodesics L_H and L_V correspond to the directivity angles α_H and α_V, respectively. Therefore, the area of the spherical rectangle is

$$S_A = 4\arcsin\left(\tan\frac{\alpha_V}{2}\tan\frac{\alpha_H}{2}\right). \tag{3}$$

As the power density at the wavefront is given by $P_R = Ar^{-\zeta}$, the antenna directivity gain corresponding to angles α_V and α_H can be established as

$$G(\alpha_V, \alpha_H) = \frac{4\pi}{S_A} = \frac{\pi}{\arcsin\left(\tan\frac{\alpha_V}{2}\tan\frac{\alpha_H}{2}\right)}, \tag{4}$$

which leads to $A = P_T G\left(\alpha_{T,V}, \alpha_{T,H}\right) G\left(\alpha_{R,V}, \alpha_{R,H}\right)$.

Hence, the received power takes the following form

$$P_R(r) = \frac{\left[\arcsin\left(\tan\frac{\alpha_{V,R}}{2}\tan\frac{\alpha_{H,R}}{2}\right)\right]^{-1}}{\arcsin\left(\tan\frac{\alpha_{V,T}}{2}\tan\frac{\alpha_{H,T}}{2}\right)} P_T\pi^2 r^{-\zeta}, \tag{5}$$

where one can determine the path loss exponent ζ for a particular technology by using empirical data, see, e.g., [34] for the frequency range of $0.5 - 100$GHz. Note that for simplicity we assume no power control on the end nodes.

C. Metrics of Interest

Our considered metrics are the first moments of aggregate interference and SIR. In particular, SIR is one of the fundamental metrics in wireless communications that characterizes the channel conditions and affects many wireless system parameters, such as the choice of the modulation and coding scheme [35], [36]. Notably, in practical systems, the knowledge of SIR value is mapped onto the modulation and coding scheme that is used at the air interface. We specifically note that the developed methodology can also be used to obtain moments of other metrics, including spectral efficiency, capacity, etc.

TABLE I
NOTATION USED IN THIS PAPER.

Parameter	Definition	Parameter	Definition
λ	Spatial density of Rx nodes	μ_I, σ_I^2	Mean and variance of interference
R_i, T_i	i-th Rx/Tx	μ_{P_R}	Mean received power
H_R, H_T	Rx/Tx heights	$K_{P_R,I}$	Covariance between interference/received power
$1/\mu_R, 1/\mu_T$	Mean height of Rx/Tx	$E[I_1^n]$	Moments of interference from an interferer
R_T	Maximum distance between Tx and Rx	$p_C(r)$	Directional exposure probability at distance r
R_I	Interference radius around the tagged Rx	$p_V(r)$	Vertical exposure probability at distance r
r_B, H_B	Communication entity's radius and height	$p_H(r)$	Planar exposure probability at distance r
$1/\mu_B$	Mean communication entity's height	$p_B(r)$	Blockage probability at distance r
λ_B	Spatial density of blockers	$\Gamma(z)$	Euler Gamma function
N	Number of interferers	J_n^z	Bessel function of the first kind
$L_P(r)$	Path loss at distance r	$E_n(x)$	Exponential integral function
ζ	Path loss exponent	H_n^z	Struve function
P_T, P_R	Transmit and receive power	G_r	Difference between LoS and blocker heights
A	Factor accounting for Tx power and gains	ξ_i, η_i	Auxiliary variables
$\alpha_{T,H}, \alpha_{T,V}$	Planar and vertical Tx antenna directivities	$\mathbb{J}$	Jacobian of transformation
$\alpha_{R,H}, \alpha_{R,V}$	Planar and vertical Rx antenna directivities	$\{\gamma, \theta, \beta\}$	Angles defining vertical exposure probability
χ	Spherical angle for wavefront density	H_{IT}, H_{IR}	Heights of interfering Tx/Rx pair
L_H, L_V	Spherical geodesics	d_T, d_I	Distances to the tagged and interfering Tx nodes
ρ	Spherical excess of a rectangle	$f_X(x)$	Probability density function of RV X
S_A	Surface area of a wavefront	$f_{\vec{X}}(\vec{x})$	Joint probability density function of RVs $\vec{X}$
I	Aggregate interference	$\vec{x}^n$	Vector of size n
S	Signal-to-interference ratio	x_i	Element i of vector $\vec{x}^n$, $i = 1, 2, \ldots, n$

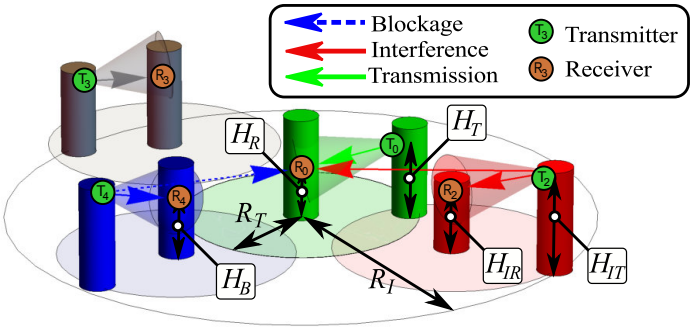

(a) Considered 3D communication scenario.

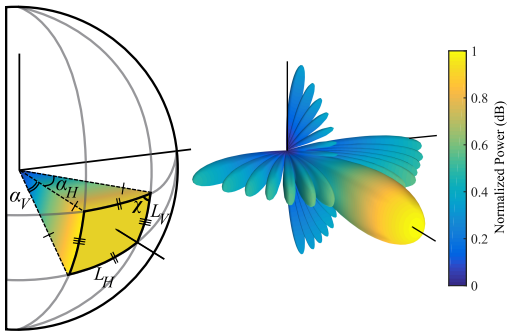

(b) Illustration of antenna radiation pattern modeling.

Fig. 1. Main system considerations.

The aggregate interference and SIR can be written as

$$I = A\sum_{i=1}^{N} d_i^{-\zeta}, \; S = \frac{Ad_0^{-\zeta}}{A\sum_{i=1}^{N} d_i^{-\zeta}} = \frac{d_0^{-\zeta}}{\sum_{i=1}^{N} d_i^{-\zeta}}, \quad (6)$$

where N is a Poisson random variable (RV) with the mean of $\lambda\pi R_I^2$, while d_i, $i = 1, 2, \ldots, N$, are the distances in $\Re^3$ between the Rx of interest and the interfering Tx nodes.

Our system model assumptions are summarized in Table II. Below, we analyze the system under these assumptions. In subsection IV-D, we relax some of them by showing how our framework can be extended to accommodate additional submodels.

IV. Performance Analysis

In this section, we evaluate the SIR in the introduced 3D mmWave deployment. First, we provide an approximation for the mean SIR by using a Taylor series expansion. Next, we proceed with establishing the main results required to determine the SIR. Finally, we describe the special cases of the proposed model that can be considered as candidates for a suitable approximation.

A. SIR Approximation

To obtain the mean SIR, we apply a Taylor series expansion of the SIR function $S = g(x, y) = P_R/I$. A second-order

TABLE II
SUMMARY OF SYSTEM ASSUMPTIONS.

Consideration	Assumption
Rx deployment	Poisson point process in $\Re^2$
Tx deployment	Uniform distribution in a circle of radius R_T around Rx
Rx height	Exponential distribution
Tx height	Exponential distribution
Blocker model	Cylinder with constant base radius and exponentially distributed height
Propagation model	UMi Street-Canyon LoS model converted to $Ar^{-\zeta}$ model
Blockage model	Binary LoS blockage model ("zero-interference" when LoS is blocked)
Radiation pattern model	Pyramidal (constant power density at base, no density outside)
Antenna sensitivity model	Pyramidal (constant power density at base, no density outside)
Metric of interest	Signal-to-interference ratio (SIR)

approximation is obtained by expanding $g(x,y)$ around $\vec{\mu} = (E[P_R], E[I]) = (\mu_{P_R}, \mu_I)$, which leads to [37]

$$E[g(\vec{\mu})] \approx g(\vec{\mu}) + \frac{g''_{xx}(\vec{\mu})\sigma^2_{P_R} + 2g''_{xy}K_{P_R,I} + g''_{yy}(\vec{\mu})\sigma^2_I}{2}, \quad (7)$$

where $K_{P_R,I}$ is the covariance between P and I, while $\sigma^2_{P_R}$ and σ^2_I are the variances of P_R and I, respectively.

Observing that

$$g''_{xx}(x,y) = 0,\ g''_{x,y}(x,y) = -y^{-2},\ g''_{yy}(x,y) = 2x/y^2, \quad (8)$$

we arrive at the following approximation

$$E[P_R/I] \approx \frac{\mu_{P_R}}{\mu_I} - \frac{K_{P_R,I}}{\mu^2_I} + \frac{\sigma^2_I \mu_{P_R}}{\mu^3_I}. \quad (9)$$

The moments of the aggregate interference are obtained by using the Campbell's theorem [38]

$$E[I^n] = \int_0^{R_I} E[I_1^n(r)] p_C(r)[1 - p_B(r)] 2\lambda\pi r dr, \quad (10)$$

where $2\lambda\pi r dr$ is the probability of having an interferer in the infinitesimal increment of the circumference dr, $p_C(r)$ is the probability that the transmit antennas of the interfering Tx nodes are oriented such that they contribute to the interference at the Rx (named here the exposure probability), $p_B(r)$ is the probability that the LoS path is being blocked by some Tx or Rx nodes, and $E[I_1^n(r)]$ are the moments of the interfering signal from a single interferer conditioned on the distance between the Rx and the interferer.

B. Main Results

To obtain the mean SIR, the following are required: (i) the mean received power, $\mu_{P_R} = E[P_R]$, (ii) the first two conditional moments of the interference power from a single interferer, $E[I_1^n]$, $n = 1, 2, \ldots$, (iii) the exposure probability, p_C, (iv) the blockage probability conditioned on the distance r, $p_B(r)$, and (v) the covariance between the received power and the interference power, $K_{P_R,I}$. The propositions below establish these quantities.

Proposition 1 (Mean Received Power)**.** *The moments of the received signal power are given as*

$$E[P_R^n] = A^n 2^{\frac{1}{2}-\zeta n} \left[W(\mu_T, \mu_R) + W(\mu_R, \mu_T)\right] \times \times \frac{\pi^{\frac{3}{2}} \csc\left(\frac{\pi\zeta n}{2}\right) \sec\left(\frac{\pi\zeta n}{2}\right) R_T^{-\left(\frac{n\zeta-5}{2}\right)}}{\mu_R^2 \mu_T^2 (\mu_R + \mu_T)\, \Gamma\left(\frac{n\zeta}{2}\right) \Gamma\left(\frac{n\zeta-1}{2}\right)}, \quad (11)$$

where $W(x,y)$ is given by

$$W(x,y) = x^3 \Big[2\sqrt{2} y^{\zeta n} R_T^{\frac{n\zeta+1}{2}} + R_T^2 2^{\frac{\zeta n}{2}} y^{\frac{n\zeta+3}{2}} \Gamma\left(\frac{n\zeta-1}{2}\right) \times \times \left(\cos\left(\frac{\pi\zeta n}{2}\right) H^{yR_T}_{\frac{3-n\zeta}{2}} - J^{yR_T}_{\frac{n\zeta-3}{2}} - \sin\left(\frac{\pi\zeta n}{2}\right) J^{yR_T}_{\frac{3-n\zeta}{2}} \right) \Big],$$

where $\Gamma(z)$ is the Euler Gamma function, J_n^z is the Bessel function of the first kind, and H_n^z is the Struve function.

Proof. The power of the received signal may be expressed as

$$P_R = A \left(\sqrt{(H_T - H_R)^2 + r^2} \right)^{-\zeta}, \quad (12)$$

where H_T, H_R, and r are the RVs.

The pdf of $|H_T - H_R|$ is known to be

$$f_{|H_T - H_R|}(y) = \frac{(e^{-y\mu_R} + e^{-y\mu_T})\mu_R\mu_T}{\mu_R + \mu_T},\ y > 0. \quad (13)$$

Then, the sought moments, $E[P_R^n(r)]$, $n = 1, 2, \ldots$, of the received signal power can be established as in [39]

$$E[P_R^n] = \int_0^{R_T} \int_0^{\infty} \frac{A^n \left(e^{-y\mu_R} + e^{-y\mu_T}\right) \mu_R \mu_T 2r}{\left(r^2 + y^2\right)^{\frac{n\zeta}{2}} (\mu_R + \mu_T) R_T^2} dy dr. \quad (14)$$

Evaluating the integrals in (14), we arrive at (11). □

The obtained result immediately leads to the following corollary, which delivers the conditional moments of interference power from a single interferer.

Corollary 1 (Conditional Moments of Interference Power from a Single Interferer)**.** *The conditional moments of interference are produced directly from (14) by fixing the planar distance between the interferer and the Rx, r, and assume the form of*

$$E[I_1^n(r)] = \frac{\left[W_1(\mu_T) + W_1(\mu_R)\right] \left[(\mu_R + \mu_T)\, \Gamma\left(\frac{n\zeta}{2}\right)\right]}{2^{-\frac{n\zeta+1}{2}} A^n \pi^{\frac{3}{2}} \mu_R \mu_T}, \quad (15)$$

where $W_1(x)$ is given by

$$W_1(x) = \left[\frac{r}{x}\right]^{\frac{1-n\zeta}{2}} \Big[2J^{rx}_{\frac{n\zeta-1}{2}} \csc(n\pi\zeta) - - J^{rx}_{\frac{1-n\zeta}{2}} \sec\left(\frac{n\pi\zeta}{2}\right) + \csc\left(\frac{n\pi\zeta}{2}\right) H^{rx}_{\frac{1-n\zeta}{2}} \Big]. \quad (16)$$

To determine the LoS blockage probability, we introduce the so-called LoS blockage zone, $ABCD$, as shown in Fig. 2. Whenever at least one center of a blocker falls into this zone,

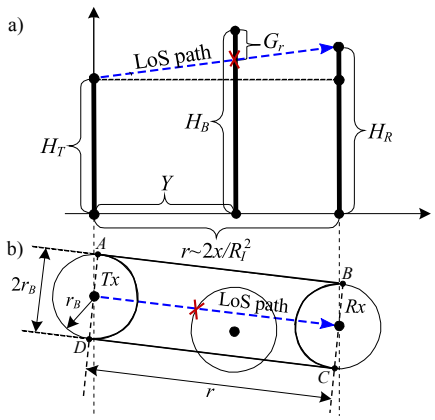

Fig. 2. Illustration of blockage in three dimensions.

the LoS path becomes occluded. The blockage probability $p_B(r)$ is established in the following proposition, while Fig. 2 illustrates the proof.

Proposition 2 (Blockage Probability)**.** *The blockage probability in a Poisson field of blockers with exponentially distributed heights of the Tx and Rx nodes is established as*

$$p_B(r) = 1 - \left(\frac{\mu_R \mu_T}{(\mu_B + \mu_R)(\mu_B + \mu_T)} \right)^{\frac{2r_B r \lambda \mu_R \mu_T}{\mu_B(\mu_B+\mu_R+\mu_T)}}. \quad (17)$$

Proof. Let G_r, $0 < r < R_I$, be the RV denoting the difference between the height of the LoS path and the blocker height H_B at planar distance r from the Tx. Observe that the centers of blockers falling into the LoS blockage zone are distributed uniformly over $(0, R_I)$. Assuming $H_R \geq H_T$, we have

$$G_r = \frac{(H_R - H_T)Y}{r} + H_T - H_B, \quad (18)$$

where H_T, H_B, and H_R are the RVs with known pdfs, Y is the RV that is distributed uniformly in $(0, r)$. Note that in case of $H_R < H_T$, one needs to replace the RV Y with $(r - Y)$. However, as long as Y remains distributed uniformly in $(0, r)$, the RV $(r - Y)$ is distributed as Y.

The probability that a single blocker located at the distance of r from the Rx occludes the LoS path is delivered by

$$p_{B,1}(r) = 1 - Pr\left\{ \frac{(H_R - H_T)Y}{r} + H_T - H_B > 0 \right\}. \quad (19)$$

Knowing $p_{B,1}(r)$ and applying the properties of the Poisson process, we establish the overall blockage probability as

$$p_B(r) = 1 - \sum_{i=0}^{\infty} \frac{(2\lambda r_B r)^i}{i! e^{2\lambda r_B r}} [1 - p_{B,1}(r)]^i = \\ = 1 - e^{-2\lambda r_B r} - \sum_{i=1}^{\infty} \frac{(2\lambda r_B r)^i}{i! e^{2\lambda r_B r}} [1 - p_{B,1}(r)]^i, \quad (20)$$

where $p_{B,1}(r) = Pr\{G_r - H_B > 0\}$ is the unknown term.

Let $\vec{\xi}^n = \{\xi_1, \xi_2, \xi_3, \xi_4\} = \{H_B, H_R, H_T, Y\}$ where the joint pdf (jpdf) of

$$f_{\vec{\xi}^n}(\vec{x}^n) = \frac{\mu_B e^{-\mu_B x_1} \mu_R e^{-\mu_R x_2} \mu_T e^{-\mu_T x_3}}{r}, \quad (21)$$

and define $\{\eta_1\} = \{G_r\}$ as the target variable. Supplementing with auxiliary variables

$$\vec{\eta}^n = \{\eta_1, \eta_2, \eta_3, \eta_4\} = \{G_r, H_R, H_T, Y\}, \quad (22)$$

the transformation at hand reads as

$$y_1 = f(\vec{x}^n) = G_r = \frac{(x_2 - x_3)x_4}{r} + x_3 - x_1, \quad (23)$$

where the auxiliary functions are $f_i(x^n) = x_i$, $i \in \{2, 3, 4\}$.

Note that the inverse transformation is a bijection

$$x_1 = \phi_1(\vec{y}^n) = -\frac{ry_1 - ry_3 - y_2 y_4 + y_3 y_4}{r},$$

which is complemented with $x_i = \phi_i(\vec{y}^n) = y_i$, $i \in \{2, 3, 4\}$.

Then, the jpdf can be represented as

$$f_{\vec{\eta}^n}(\vec{y}^n) = f_{\xi^n}(\phi_1(\vec{y}^n), \ldots, \phi_n(\vec{y}^n))|\mathbb{J}|, \quad (24)$$

where $f_{\vec{\xi}^n}(\phi_1(\vec{y}^n), \ldots, \phi_n(\vec{y}^n))$ can be established as

$$f_{\vec{\xi}^n}(\vec{\phi}^n(\vec{y}^n)) = \frac{\mu_R \mu_T \mu_B}{r} \times \\ \times e^{\frac{\mu_B(ry_1 - ry_3 - y_2 y_4 + y_3 y_4)}{r} - y_2 \mu_R - y_3 \mu_T}, \quad (25)$$

and the Jacobian is $\mathbb{J} = \partial \phi_1(\vec{y}^n) / \partial y_1 = -1$.

The pdf of G_r can now be written as in (26), where

$$l_1(\vec{y}^n) = \max\left\{0, \frac{y_2 y_3 - r y_2}{y_3}, \frac{-r y_2 + r y_4 + y_2 y_3}{y_3}\right\}, \quad (27)$$

and the final integrand takes the following form in (28).

Evaluating the integral in (26) is not feasible in the closed form. However, after changing the order of integration, we arrive at

$$p_{B,1}(r) = 1 - \int_0^r \int_0^\infty f_{\eta_1 \eta_4}(y_1, y_4) dy_1 dy_4 = \\ = \frac{\mu_R \mu_T \log\left(\frac{\mu_R \mu_T}{(\mu_B + \mu_R)(\mu_B + \mu_T)}\right)}{\mu_B(\mu_B + \mu_R + \mu_T)}. \quad (29)$$

Substituting (29) into (20) and simplifying, yields (17). □

Observing Fig. 3 one may deduce that the directional exposure probability at the planar distance of r between the Rx and the interferer, $p_C(r)$, can be found as

$$p_C(r) = p_V(r) p_H(r), \quad (30)$$

where $p_H(r)$ is the probability that the interferer exposes the tagged Rx on the horizontal plane, $p_V(r)$ is the probability that this also occurs in the third dimension. Following [11], the planar exposure probability is produced by

$$p_H(r) = \frac{\alpha_{T,H} r}{2\pi r} \frac{\alpha_{R,H} r}{2\pi r} = \frac{\alpha_{T,H} \alpha_{R,H}}{4\pi^2}, \quad (31)$$

where $\alpha_{T,H}$ and $\alpha_{R,H}$ are the planar directivities at Tx and Rx, respectively. The vertical exposure to interference is demonstrated in Fig. 3(a). The following proposition establishes the vertical exposure probability.

$$f_{\eta_1}(y_1)=\iiint\limits_{\mathrm{R}^3} f_{\vec{\xi}^n}[\phi_i(\vec{y}^n)]|\mathbb{J}|dy_2dy_3dy_4=\int\limits_0^r\int\limits_0^\infty\int\limits_{l_1(\vec{y}^n)}^\infty \frac{\mu_R\mu_T\mu_B}{r}e^{\frac{\mu_B(ry_1-ry_3-y_2y_4+y_3y_4)}{r}-y_2\mu_R-y_3\mu_T}dy_2dy_3dy_4=$$
$$=\int\limits_0^r\int\limits_0^\infty \frac{\mu_R\mu_T\mu_B}{r\mu_R+\mu_By_4}e^{\frac{r\mu_By_1-ry_3(\mu_T+\mu_B)+\mu_By_3y_4-(r\mu_R+\mu_By_4)\max\left\{0,r(y_1-y_3)y_4^{-1}+y_3\right\}}{r}}dy_3dy_4=\int\limits_0^r f_{\eta_1\eta_4}(y_1,y_4)dy_4. \quad (26)$$

$$f_{\eta_1\eta_4}(y_1,y_4)=-\frac{(y_4\mu_B+r\mu_R)^{-1}\,e^{-\frac{ry_1\mu_R}{y_4}-\frac{ry_1\mu_T}{r-y_4}}\,\mu_B\mu_R\mu_T}{(r\mu_B-y_4\mu_B+r\mu_T)\,(-r\mu_R+y_4\mu_R+y_4\mu_T)}\times \quad (28)$$
$$\times\Big(-e^{\frac{ry_1\mu_T}{r-y_4}}ry_4\mu_B+e^{\frac{ry_1\mu_T}{r-y_4}+ry_1\left(\frac{\mu_R}{y_4}+\frac{\mu_T}{-r+y_4}\right)}ry_4\mu_B+e^{\frac{ry_1\mu_T}{r-y_4}}y_4^2\mu_B-e^{\frac{ry_1\mu_T}{r-y_4}+ry_1\left(\frac{\mu_R}{y_4}+\frac{\mu_T}{-r+y_4}\right)}y_4^2\mu_B+$$
$$+e^{\frac{ry_1\mu_R}{y_4}}r^2\mu_R-e^{\frac{ry_1\mu_R}{y_4}}ry_4\mu_R-e^{\frac{ry_1\mu_R}{y_4}}ry_4\mu_T-e^{\frac{ry_1\mu_T}{r-y_4}}ry_4\mu_T+e^{\frac{ry_1\mu_T}{r-y_4}+ry_1\left(\frac{\mu_R}{y_4}+\frac{\mu_T}{-r+y_4}\right)}ry_4\mu_T\Big).$$

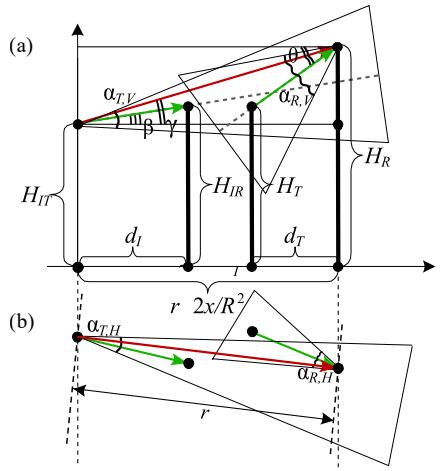

Fig. 3. Directional exposure for directional Tx and Rx nodes.

Proposition 3 (Vertical Exposure Probability)**.** *The vertical exposure probability in a system with directional Tx and Rx nodes is given by*

$$p_V(r)=\int\limits_{-\infty}^{\infty}\int\limits_{y_4-\frac{\alpha_{T,V}}{2}}^{y_4+\frac{\alpha_{T,V}}{2}}\int\limits_{y_4-\frac{\alpha_{R,V}}{2}}^{y_4+\frac{\alpha_{R,V}}{2}} f_{\gamma,\theta,\beta}\,(y_1,y_4,y_6)dy_1dy_6dy_4, \quad (32)$$

where $f_{\gamma,\theta,\beta}\,(y_1,y_4,y_6)$ is the jpdf of the angles $\{\theta,\gamma,\beta\}$, see Fig. 3, while $\alpha_{T,V}$ and $\alpha_{R,V}$ are the vertical directivities at Tx and Rx, respectively.

Proof. Consider the system of RVs $\{\theta,\gamma,\beta\}$, see Fig. 3, where θ is the angle at which the beam arrives to the tagged Rx from the tagged Tx, γ is the angle at which the LoS between the tagged Rx and the interferer rises above the horizon, and β is the angle at which the beam is directed from a non-tagged Tx to its associated Rx. Using $\alpha_{T,V}$ and $\alpha_{R,V}$ as the vertical directivities of the Tx and the Rx, the vertical exposure probability is characterized by (32).

Let us relabel the input RVs as

$$\vec{\xi}^n=\{\xi_1,\xi_2,\ldots,\xi_6\}=\{H_T,H_R,d_T,H_{IT},d_I,H_{IR}\}, \quad (33)$$

where H_T and H_R are the heights of the Tx and the Rx, respectively, H_{IT} and H_{IR} are the heights of the Tx and the Rx associated with the interfering radio link, while d_T and d_I are the planar distances between the tagged and the interfering communicating pairs. The jpdf of ξ_1^n has the following multiplicative form

$$f_{\vec{\xi}^n}\,(\vec{x}^n)=\frac{4x_3x_5\mu_T^2\mu_R^2}{R_T^4}e^{-\mu_Tx_1-\mu_Rx_2-\mu_Tx_4-\mu_Rx_6}, \quad (34)$$

which is due to independence of the involved RVs.

We also relabel the set of target RVs as

$$\vec{\eta}^m=\{\eta_1,\eta_4,\eta_6\}=\{\theta,\gamma,\beta\}, \quad (35)$$

and since the number of the target RVs, m, is lower than the number of the input RVs, n, we supplement them with the auxiliary RVs as

$$\vec{\eta}^n=\{\eta_1,\eta_2,\ldots,\eta_6\}=\{\theta,H_R,d_T,\gamma,d_I,\beta\}. \quad (36)$$

Further, the transformation in question and complementary auxiliary functions are given by

$$\begin{cases} y_1=f_1\,(\vec{x}^n)=\theta=\tan^{-1}\left(\frac{x_1-x_2}{x_3}\right),\\ y_4=f_4\,(\vec{x}^n)=\gamma=\tan^{-1}\left(\frac{x_4-x_2}{r}\right),\\ y_6=f_6\,(\vec{x}^n)=\beta=\tan^{-1}\left(\frac{x_4-x_6}{x_5}\right),\end{cases}\quad \begin{cases} y_2=f_1\,(\vec{x}^n)=x_2,\\ y_3=f_3\,(\vec{x}^n)=x_3,\\ y_5=f_5\,(\vec{x}^n)=x_5.\end{cases} \quad (37)$$

Note that the inverse transformation is a bijection within the domain of θ, γ, and $\beta=(-\pi/2,\pi/2)$. Hence, the inverses are

$$\begin{cases} x_1=\phi_1\,(\vec{y}^n)=y_2+y_3\tan y_1,\\ x_4=\phi_4\,(\vec{y}^n)=y_2+r\tan y_4,\\ x_6=\phi_6\,(\vec{y}^n)=y_4+y_5\tan y_6,\end{cases}\quad \begin{cases} x_2=\phi_2\,(\vec{y}^n)=y_2,\\ x_3=\phi_3\,(\vec{y}^n)=y_3,\\ x_5=\phi_5\,(\vec{y}^n)=y_5.\end{cases} \quad (38)$$

As a result, the sought jpdf may be written as

$$f_{\vec{\eta}^n}\,(\vec{y}^n)=\iiint\limits_{\mathrm{R}^3} f_{\vec{\xi}^n}(\phi_1(\vec{y}^n),\ldots,\phi_n(\vec{y}^n))|\mathbb{J}|dy_2dy_5dy_3, \quad (39)$$

where the Jacobian is computed by

$$\mathbb{J}=-ry_3y_5\sec^2\,(y_1)\sec^2\,(y_4)\sec^2\,(y_6)\,, \quad (40)$$

and the integrand is available as

$$f_{\vec{\xi}^n}(\vec{\phi}^n(\vec{y}^n)) = \frac{4y_3y_5\mu_R^2\mu_T^2}{R_T^4} e^{-y_2\mu_R-\mu_T(y_2+y_3\tan[y_1])}\times \\ \times e^{-\mu_T(y_2+x\tan[y_4])-\mu_R(y_4-y_5\tan[y_6])}. \quad (41)$$

Performing the integration, we arrive at (42), where

$$h_1 = \max\{0, -y_4\cot(y_1), -r\tan(y_4)\}, \\ h_2 = \max\{0, -y_3\tan(y_1), -r\tan(y_4)\}. \quad (43)$$

Here, the latter two integrals can also be taken, which leads to a closed-form expression for $f_{\gamma,\theta,\beta}(y_1, y_4, y_6)$. The final form of the target jpdf is provided in Supplement[1]. □

Note that the numerical integration according to (32) is computationally challenging. The corresponding details are provided in Appendix A.

Proposition 4 (Covariance $K_{P_R,I}$)**.** *The covariance between the interference and the received signal powers is given*

$$E[P_RI] = A^2\lambda\pi R_I^2 p_C E[(X_iX_0)^{-\zeta}], \quad (44)$$

and $E[(X_0X_i)^{-\zeta}]$ is obtained by the numerical integration of

$$\int_0^{R_I}\int_0^{R_T}\int_0^{\infty}\int_0^{\infty}\int_0^{\infty} \frac{[(x_1-x_2)^2+x_5^2]^{-\frac{\zeta}{2}}}{[(x_1-x_3)^2+x_4^2]^{\frac{\zeta}{2}}} f(x_1,..,x_5)dx_1..dx_5, \quad (45)$$

with the associated jpdf in the following form

$$f(x_1,\ldots,x_5) = \frac{\mu_T\mu_R^2 e^{-\mu_T x_1-\mu_R(x_2+x_3)}4x_4x_5}{(R_TR_I)^2}. \quad (46)$$

Proof. By formulating $K_{P_R,I} = E[P_RI] - \mu_{P_R}\mu_I$, we have

$$E[P_RI] = E\Big[AX_0^{-\zeta}\sum_{i=1}^{N} AX_i^{-\zeta}\Big], \quad (47)$$

where X_0 is the distance between the Tx and the tagged Rx, X_i, $i = 1, 2, \ldots, N$, are the distances between the interferers and the Rx, and N is the number of interferers.

Applying the Wald's identity [39] yields

$$E[P_RI] = A^2E[N]E[(X_iX_0)^{-\zeta}], \quad (48)$$

where $E[N] = \lambda\pi R_I^2 p_C$, $E[(X_0X_i)^{\zeta}]$ are the only unknowns.

Therefore, we rewrite $E[(X_0X_i)^{-\zeta}]$ as

$$E[([(H_R-H_T)^2-r_0][(H_R-H_I)^2-r_i])^{-\frac{\zeta}{2}}], \quad (49)$$

where r_0 is a constant, and consequently arrive at (44). □

Note that the computational complexity of the numerical integration depends on the integration order. By choosing it as in (45), the said complexity may be reduced to the sum of single integrals, which can be easily evaluated numerically.

[1]Supplement A [Available online]: http://winter.rd.tut.fi/supplement.pdf

C. Special Cases of the Model

Our proposed 3D model includes a number of cases of particular interest that are characterized by different computational complexity. As these simpler models can be efficiently utilized to approximate the SIR for certain limited ranges of system parameters, we summarize them in what follows.

1) Directional Tx Nodes and Omnidirectional Rx Nodes

Mobile terminals are not expected to feature more than several antennas, which implies that their sensitivity and antenna directivity might not be too high. At the same time, assuming omnidirectional antennas at one end of the radio communication link permits for a drastic decrease in computational complexity for the considered model. The critical difference between the proposed 3D model and a model with omnidirectional sensitivity at the Rx nodes lies in treating the exposure probability. The planar exposure probability is immediately delivered by $p_H(r) = \alpha/2\pi$, while the vertical exposure probability is derived in Appendix B.

2) Fixed Heights of Communicating Entities

In certain mmWave-based scenarios, the heights of the communicating entities are known in advance. In this case, the heights of the Tx and Rx nodes can be fixed, which leads to a significant simplification of the model. Another application of this formulation is by approximating the original model having random heights with the use of the mean heights. The main difference between the proposed model and this simplification is in the exposure and blockage probabilities. The propositions that establish these components are provided in Appendix B. Since the vertical exposure probability can be made available in the closed form, the computational complexity of the model with fixed heights is much smaller.

3) Fully Planar Model

This model is the simplest case, where both the interference and the SIR can be expressed with the help of an exponential integral function. The primary difference between the 3D model and the planar case is in the probability of blockage, $p_B(r)$, as well as the exposure probability, $p_C(r)$. Accordingly, $p_C(r)$ reduces to $p_C(r) = (\alpha_T\alpha_R)/4\pi^2$, where α_T and α_R are planar antenna directivities. Further, the blockage probability in the planar model can be approximated by the probability that the center of at least one blocker falls into the LoS blockage zone having the sides of $2r_B$ and X, where X is the RV with the pdf of $f_X(x) = 2x/R_T^2$, see Fig. 2(b). The conditional blockage probability is given by the void probability of the spatial Poisson process, see e.g., [6]

$$p_B(r) = e^{-2\lambda r_B r}. \quad (50)$$

Using (10), the moments of interference are expressed as

$$E[I^n] = \int_{r_B}^{R_I} (Ar^{-\zeta})^n(1-e^{-2\lambda r_B r})\frac{\alpha}{2\pi}2\lambda\pi r dr = \\ = A^n\alpha\lambda\Big[\frac{E_{n\zeta-1}(-2\lambda r_B^2)}{r_B^{\zeta n-2}} - \frac{E_{n\zeta-1}(-2\lambda r_B R_I)}{R_I^{\zeta n-2}}\Big], \quad (51)$$

where $E_n(x)$ is the exponential integral function [40].

$$f_{\vec{\eta}^n}(\vec{y}^n) = \tag{42}$$
$$= \int_0^{R_T}\int_{h_1}^{R_T}\int_{h_2}^{\infty} \frac{4ry_3^2y_5^2\mu_R^2\mu_T^2 \sec {y_1}^2 \sec {y_4}^2 \sec {y_6}^2}{R_T^4} e^{-y_2\mu_R-\mu_T(y_2+y_3\tan y_1)-\mu_T(y_2+r\tan y_4)-\mu_R(y_4-y_5\tan y_6)} dy_2 dy_5 y_3 =$$
$$= \int_0^{R_T}\int_{h_1}^{R_T} \frac{4ry_3^2y_5^2\mu_R^2\mu_T^2 \sec {y_1}^2 \sec {y_4}^2 \sec {y_6}^2}{R_T^4(\mu_R+2\mu_T)} e^{-y_4\mu_R-(\mu_R+2\mu_T)h_2-y_3\mu_T\tan[y_1]-r\mu_T\tan[y_4]+y_5\mu_R\tan[y_6]} dy_5 dy_3.$$

Finally, the mean can be evaluated by using (9), where $K_{P,I} = 0$ for the 2D case, while the moments of interference are delivered by (51) and the mean received signal is then

$$E[P_R] = \int_{r_B}^{R_T} Ax^{-\zeta}\frac{2x}{R_T^2}dx = \frac{2A\left(r_B^{2-\zeta} - R_T^{2-\zeta}\right)}{(\zeta-2)R_T^2}. \tag{52}$$

D. Extensions of the Model

The system analyzed in this section follows the assumptions summarized in Table II. However, some of those can be relaxed, thus allowing to capture more complex environments. Below, we briefly summarize the feasible extensions of our model.

One of the critical assumptions is the exponential distribution of Tx, Rx, and blocker heights. The rationale behind this consideration is the analytical tractability of the exponential distribution and the lack of data on heights of practical mmWave-based entities. However, as verified by the authors, one may use any distribution characterized by an exponential function with constants. This class includes Laplace, Gaussian, and Uniform distributions that may potentially provide better approximations in specific scenarios of interest.

The developed framework assumes zero power density and sensitivity outside of the half-power beamwidth (HPBW) of the antenna radiation/sensitivity pattern. A straightforward extension would be to use the pyramid with sphere abstraction tackled in [11]. Another crucial assumption of our approach is the use of UMi Street-Canyon model, which leads to "zero-interference" conditions when blockers occlude the LoS path. Although the framework in its current form cannot be extended to an algorithmic 3GPP cluster-based model originally proposed in [41], one may capture non-zero interference by using two power law propagation models in the form of $A_i e^{-\zeta_i}$, $i = 0, 1$, where 0 and 1 correspond to LoS and nLoS conditions. In this case, (10) takes the following form

$$E[I^n] = \int_0^{R_I} E[I_{1,0}^n(r)]p_C(r)[1-p_B(r)]2\lambda\pi r dr + \\ + \int_0^{R_I} E[I_{1,1}^n(r)]p_C(r)p_B(r)2\lambda\pi r dr, \tag{53}$$

where $E[I_{1,0}^n]$ and $E[I_{1,1}^n]$ are the moments of interference from a single interferer conditioned on the distance between the Rx and the interferer as well as on the event that the LoS path is non-blocked and blocked, respectively. The quantities in question are obtained similarly to $E[I_1^n]$ in Proposition 1.

On top of the basic model, our developed framework is flexible enough to account for additional considerations related to blockage. First, one may capture the effect of an additional Poisson field of blockers by increasing the blocker intensity in Proposition 2. Self-blockage is captured by introducing an additional multiplier to the Campbell expression in (10). Similarly, one may extend our model to account for blockage by large static objects, such as buildings. Particularly, one may use the following blockage probability provided by 3GPP in [34]

$$p_L(r) = \begin{cases} 1, & r \le 18 \text{ m} \\ \left(18 + re^{-\frac{r}{36}} - 18e^{-\frac{r}{36}}\right)/x, & r > 18 \text{ m} \end{cases}, \tag{54}$$

where r is the two-dimensional distance between Tx and Rx.

The methodology proposed in our paper can also be employed to obtain other metrics of interest, which includes SINR, spectral efficiency, and Shannon channel capacity. As an example, consider the Shannon capacity function, $C = f(P, I) = B\log_2(1 + P/I)$. In this case, the second-order Taylor approximation for the mean capacity takes the form

$$E[C] = \frac{2[(2+\sigma_I^2)\mu_i\ \mu_P+(2+\sigma_I^2)\mu_P^2]-B(2K_{PI}+\sigma_P^2)\mu_i^2}{2\log_2\mu_i^2\ (\mu_i+\mu_P)^2}, \tag{55}$$

where μ_P and μ_I are the mean received power and the mean interference power, respectively, σ_P^2 and σ_I^2 are the variances of the received power and the interference power, respectively, and K_{PI} is the covariance between them, while B is the bandwidth. Here, the terms required to estimate $E[C]$ are the same as those derived in this work to determine the mean SIR. Hence, knowing B one can estimate the Shannon capacity, whereas setting $B = 1$ produces spectral efficiency as well.

The framework developed in this paper cannot be used to provide the distributions of the metrics of interest. However, one can obtain higher moments, such as variance, skewness, and kurtosis, by providing a partial characterization of the respective distributions. For example, a Taylor approximation for the variance $\sigma^2[S] = P/(N + I)$ takes the following form

$$\sigma^2[S] = \frac{(N_0+\mu_I)^2\sigma_I^2 + \mu_P^2\sigma_P^2 - 2K_{PI}(N_0+\mu_I)\mu_P}{N_0+\mu_I^4}, \tag{56}$$

where N_0 is the Johnson-Nyquist noise.

Higher moments will not only provide quantitative and qualitative description of the distributions, but may also be used to produce approximations for the metrics of interest, such as coverage and outage probabilities. The latter can be

accomplished by using the Markov and Chebyshev inequalities,

$$Pr\{S \geq a\} = \frac{E[S]}{a},\ Pr\{|S - E[S]| \geq k\sigma[S]\} < \frac{1}{k^2}. \quad (57)$$

Alternatively, one can employ Hoeffding bounds [42].

V. Numerical Assessment and Examples

In this section, we conduct an extensive numerical evaluation of the proposed model. We first assess the accuracy of the developed formulation by comparing the results with those obtained by using simulations. Further, we investigate the effects of system parameters, characterize the approximation error induced by utilizing the simplified models, and report on the range of input parameters where they offer accurate approximations. Finally, we analyze the SIR performance by considering dissimilar antenna array configurations, which correspond to various deployment options in mmWave systems as well as typical use cases, including AP to UE, drone-cell to UE, and UE to UE deployments. The default parameters utilized throughout this section are summarized in Table III.

TABLE III
Considered system parameters.

Parameter	Value
Intensity of communicating pairs, λ	0.05 Tx/m^2
Path loss exponent, ζ	2.1
Blocker radius, r_B	0.3m
Carrier frequency	28GHz
Maximum distance between Tx and Rx, R_T	15m
Maximum distinguishable interference distance, R_I	150m
Mean Rx height, $E[H_R] = 1/\mu_R$	1.5m
Mean Tx height, $E[H_T] = 1/\mu_T$	5m
Vertical directivity of Tx antenna, $\alpha_{T,V}$	2°
Planar directivity of Tx antenna, $\alpha_{T,H}$	25°
Vertical directivity of Rx antenna, $\alpha_{R,V}$	25°
Planar directivity of Rx antenna, $\alpha_{R,H}$	25°
Mean blocker height, $E[H_B] = 1/\mu_B$	1.7m

A. Accuracy Assessment

The vertical exposure probability, p_V, is a critical intermediate parameter that induces the difference between the planar and the 3D model. Recalling that the estimation of p_V is also the most complicated step in the formulated model, we first assess the accuracy of approximating p_V and then proceed with illustrating the accuracy of the SIR approximation.

The value of the vertical exposure probability as a function of the distance between the Tx and the Rx as well as the Tx vertical directivity are demonstrated in Fig. 4(a). Here, the model approximates the simulation data tightly, while the values reside within the confidence intervals. One may also notice that the confidence intervals grow as the antenna directivities become smaller. The reason is that in our simulation campaign the number of experiments was set to 10^7 trials

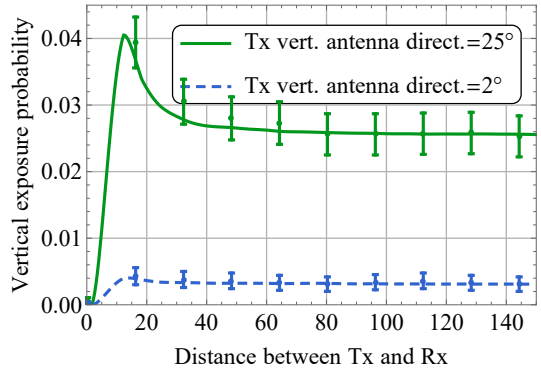

(a) Vertical exposure probability.

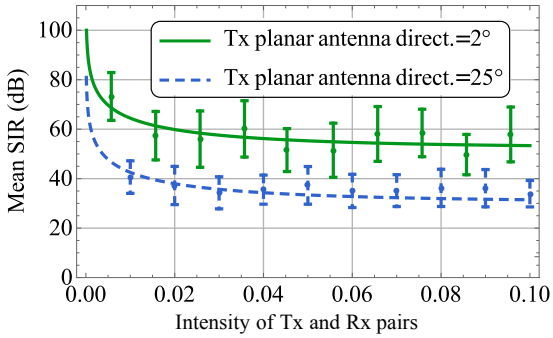

(b) Values of SIR.

Fig. 4. Results obtained with our model and simulations.

for all of the considered points. For small antenna directivity, the number of trials when the Rx is exposed is insufficient for an accurate assessment within a reasonable time, which provides additional motivation for mathematical modeling. Similar conclusions can be made by observing Fig. 4(b), which illustrates the SIR as a function of the intensity of communicating pairs and the Tx planar directivity. Hence, in what follows, we rely on the developed analytical model to showcase the response of SIR to the system parameters.

B. Effects of System Assumptions

In our study, we have adopted a number of crucial assumptions regarding the interference model, noise, and height distribution of entities. We now proceed by quantifying their effects. Fig. 5(a) illustrates the mean SIR for different distributions of heights of the communicating entities (Exponential, Laplace, Uniform, and Normal) for two Tx planar antenna directivities, 2° and 25°, as a function of the intensity of Tx and Rx pairs in the environment. To provide a fair comparison with the exponential distribution characterized by a single parameter, we assume that the standard deviation equals the mean for all the considered distributions as well. As one may notice, the type of the distribution does not affect the mean SIR drastically for the considered range of system parameters. It is interesting to note that using exponential distribution results in slightly more optimistic results.

Further, Fig. 5(b) demonstrates the mean SIR as a function of the Tx-Rx pairs intensity for two types of interference models. The first model is the "zero-interference" consideration

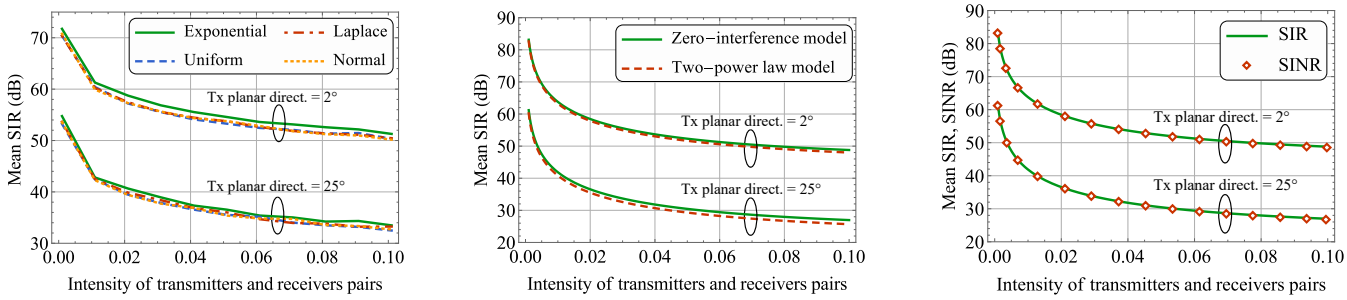

(a) The effect of height distribution. (b) The effect of blocked interference. (c) The effect of noise.

Fig. 5. The effects of noise, interference models, and height distribution.

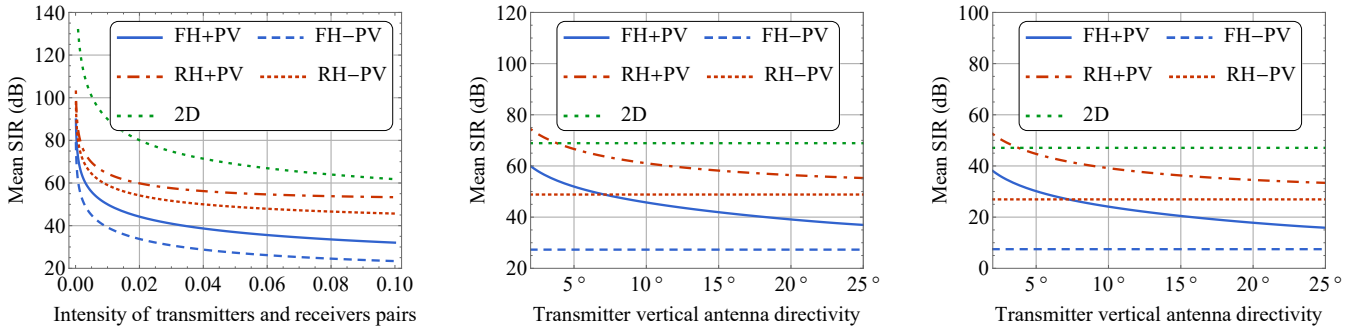

(a) Varying intensity of pairs (b) Varying $\alpha_{T,V}$, $\alpha_{T,H} = 2°$ (c) Varying $\alpha_{T,V}$, $\alpha_{T,H} = 25°$

Fig. 6. Dependence of SIR on system parameters and comparison of models.

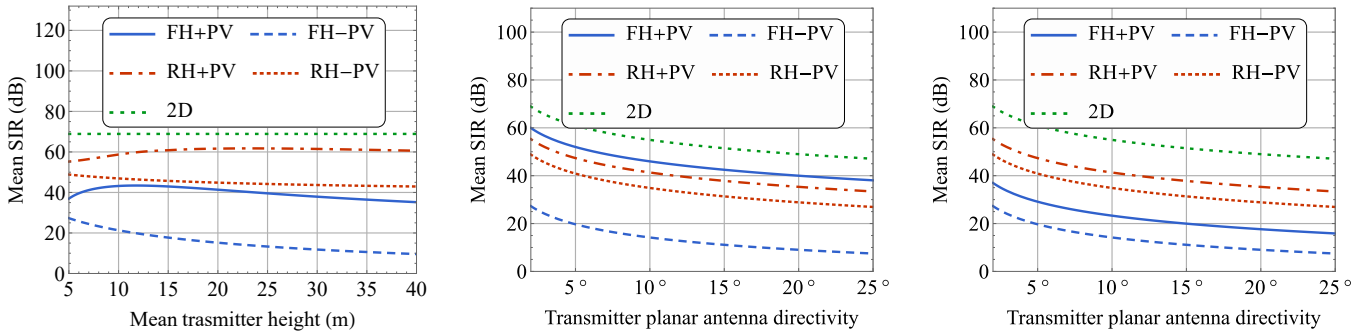

(a) Varying mean Tx height (b) Varying $\alpha_{T,H}$, $\alpha_{T,V} = 2°$ (c) Varying $\alpha_{T,H}$, $\alpha_{T,V} = 25°$

Fig. 7. Dependence of SIR on system parameters and comparison of models.

used in this paper, where we assume that no interference is produced in case of blockage. The second model is a two power law abstraction, where in case of blockage the amount of contributed interference is 7dB less as compared to the LoS case. Analyzing the data presented in Fig. 5(b), one may observe that accounting for interference created by the nodes that are currently blocked does not affect the mean SIR considerably. The reason is that the blockage probability and thus the signal power from the blocked interferers affect the total interference significantly less as compared to the exposure probability. Note that we considered how to extend our approach to the two power law interference model.

Finally, Fig. 5(c) offers a comparison between the SIR captured by our study as a parameter of interest and the SINR that also accounts for noise. First, we note that both curves are characterized by a qualitatively similar behavior. Furthermore, the introduction of noise does not result in a significant difference as compared to the SIR. The underlying reason is that the use of directional antennas in prospective mmWave systems leads to relatively high values of the received power.

C. Effects of System Parameters

Further, we analyze the effects of system parameters on the value of SIR. Our developed 3D model is characterized by high numerical complexity, which is mostly attributed to the computation of the vertical exposure probability. Therefore, it should be useful in practice to have a less sophisticated model that provides with a reasonable approximation. In this subsection, we identify the range of parameters in addition to analyzing the response of SIR to the input system parameters, where simpler models that are the special cases of the

developed 3D formulation lead to accurate approximations. In addition to a simple planar model disregarding the random heights and the vertical exposure probability, we also consider various combinations of models with fixed/random heights (FH/RH) that either take or do not take into account the vertical exposure probability ($\pm$PV). We refer to these models as FH, RH, and PV. Then, our 3D model is denoted as RH+RV. Note that all of the models include blockage. Recall that using the fixed heights and/or neglecting the vertical exposure eliminates the need for numerical integration to obtain p_V, thus making the modeling computationally simpler.

To this end, Fig. 6 depicts the SIR values for different models as a function of the two system parameters: the intensity of communicating pairs, λ, and the Tx vertical antenna directivity, $\alpha_{T,V}$. Analyzing the data outlined in Fig. 6(a), we observe that SIR decreases as the intensity of communicating pairs grows for all the considered models. This confirms that all selected models provide accurate "qualitative" description of the system at hand. Further, notice that no simpler models provide an accurate approximation of SIR across the entire range of λ.

Interestingly, the planar model that completely disregards the effects of the third dimension drastically overestimates the actual SIR performance in the system. The reason is that neglecting the heights of communicating entities dramatically increases the blockage probability, which eventually yields less interference approaching the Rx nodes. Then, three other models that partially account for the effects of the third dimension underestimate the actual SIR performance. The model taking into consideration the randomness of heights but disregarding the vertical exposure probability remains the closest to the proposed 3D model across the feasible range of intensities of the communicating pairs. The difference between these models is at most several decibels and decreases as λ becomes smaller. The least accurate model is the one with the fixed heights and the absence of vertical exposure probability.

Further, consider the effect of vertical antenna directivity as illustrated in Fig. 6(b) and Fig. 6(c) for the two values of planar antenna directivity at the Tx, $\alpha_{T,H} = 2^\circ$ and $\alpha_{T,H} = 25^\circ$. Clearly, the levels of SIR predicted by the three models that disregard the vertical exposure are independent of $\alpha_{T,V}$. For the rest of the models, higher vertical antenna directivity leads to better system performance for both considered values of planar directivities. At the same time, the model with fixed heights provides a large deviation from the actual values of the mean SIR for all the considered values of the vertical antenna directivity. Particularly, it constitutes at least 10dB for the two values of the planar directivities. For small vertical directivities within the range $(1^\circ - 5^\circ)$, the model neglecting the vertical exposure probability, coincidentally, provides an adequate approximation as we have already noticed by analyzing Fig. 6(a). This conclusion remains valid as long as the Rx antenna directivities are rather large, i.e., 20° or more. The rest of the models drastically underestimate the actual system performance.

The mean height of the Tx and the Rx are critical system parameters that affect the vertical exposure probability, p_V, and, consequently, SIR. Fig. 7(a) demonstrates the effect of the mean Tx height on the mean SIR. The mean height of the Tx affects the SIR performance only over a rather small subset of values, i.e., within the range of $1 - 10$ meters, thus implying that this parameter is important for the AP-UE communication scenarios. For others, the mean SIR remains constant. Analyzing the approximations, one may notice that only the model with fixed heights that also takes into account the vertical exposure probability captures the actual trend in the mean SIR. However, quantitatively, the two curves are approximately 20dB apart. For smaller mean Tx heights, the model with random heights that neglects the effect of p_V provides an accurate approximation, while for larger values of the mean Tx height, the results for the simplest planar model are reasonably close. We note that the impact of the mean Rx height is qualitatively similar and thus is omitted here.

We continue by considering the effect of the Tx planar directivity as illustrated in Fig. 7(b) and Fig. 7(c) for the vertical antenna directivity at the Tx of 2° and 25°, respectively. Intuitively, the higher the Tx planar directivity is, the better the system performance becomes. Furthermore, a monotonous trend is visible for both considered values of the vertical directivity. The actual SIR predicted by our developed model is in between the two models both offering reasonable approximations across the entire range of the considered planar directivities and the Tx vertical directivity of 2°: one with random heights that disregards the vertical exposure and another one with fixed heights accounting for the vertical exposure. However, for larger values of the vertical directivity, only the latter one remains adequate.

Finally, we note that the planar 2D model offers an optimistic upper bound on the SIR performance across the entire range of the input system parameters. Similarly, the model with fixed heights that neglects the vertical exposure probability is always the most pessimistic choice. The gap between these formulations can be as high as 60dB, thus implying that none of them can be used as a tight performance bound. The least computationally expensive model that provides with a reasonable approximation is the one having fixed heights and accounting for p_V. However, for certain ranges of input parameters, its prediction may still deviate by more than 10dB from the actual SIR performance.

D. SIR in Typical Communication Scenarios

By design, our developed model is capable of characterizing various types of communication scenarios. We now proceed with assessing the SIR performance of the three typical wireless setups, (i) AP to UE, (ii) Drone (UAV) to UE, and (iii) UE to UE. The scenario parameters are summarized in Table III except for the heights of the communicating entities. The mean Rx and Tx heights for the corresponding three cases are $(5, 1.5)$, $(40, 1.5)$, and $(1.5, 1.5)$, respectively.

The use of highly directional antennas at both ends of a radio link leads to challenges related to the need for efficient and accurate electronic beamtracking mechanisms [43], [44]. It is particularly important when the Tx and the Rx are mobile, and we consider three different choices of directivity at both sides of a link. The first case features 128×4 and

4×4 arrays at Tx and Rx, respectively, and is intended to model the situation for the first generation of mmWave systems. The second and the third cases are associated with $128 \times 128/4 \times 4$ and $128 \times 128/64 \times 64$ Tx/Rx arrays, and reflect further evolution of mmWave systems. To obtain the antenna directivities, we apply a well-accepted linear array approximation for the HPBW, $\alpha = 102/M$, where M is the number of antenna elements in the corresponding dimension, planar or vertical, see, e.g., [45]. We refer to these three cases as *today*, *near future*, and *distant future*.

Accordingly, Fig. 8 displays the mean SIR as a function of the intensity of communicating pairs for various antenna configurations at Tx and Rx as well as different communication scenarios. Analyzing the antenna array configurations, the gains achieved by using more sophisticated antenna design at Tx and Rx are mostly quantitative, that is, for the same intensity of communicating pairs the use of more antennas improves the SIR. It is essential that a significant improvement stems from enabling better vertical directivity at the Tx by moving from 128×4 to 128×128 array. By analyzing the data for the same antenna configurations, one may notice that the D2D (UE to UE) scenario is characterized by the worst SIR performance. This behavior is a direct consequence of having a smaller mean Tx height that increases the vertical exposure probability. The best performance across all the antenna configurations is observed for the UAV scenario. However, the difference between the Tx height of 5 and 40 meters is marginal for larger values of the intensity of communicating pairs and is becoming larger as λ decreases.

VI. Conclusions

In this work, we proposed a 3D model for the evaluation of SIR in the emerging mmWave systems, which takes into account the vertical and planar directivities at both ends of a radio link, the blockage effects in three dimensions, as well as the random heights of communicating entities. By design, our model is capable of characterizing a number of mmWave deployment scenarios, which include standard AP-based layouts, drone-assisted cases, and D2D-aided mmWave connectivity. The resulting expressions for the mean interference and SIR involve a series of integrals that cannot be solved in the closed form or expressed in terms of tabulated functions. To provide with more practical approximations, we additionally developed several simpler models having different levels of details as well as assessed their accuracy across a wide range of input system parameters.

Utilizing our developed model, we further studied in detail the response of SIR to the choice of system parameters. Particularly, we demonstrated that both the randomness of Tx and Rx heights and the vertical exposure probability are essential for accurate performance characterization of 3D mmWave deployments. The conventional planar stochastic geometry models always provide an overly optimistic output that can overestimate the mean SIR by as high as 20dB. In contrast, the model with fixed heights that disregards the effect of vertical exposure is entirely pessimistic. The range between these two extremes may approach $40 - 60$dB, thus prohibiting their use as tight upper or lower bounds. The other model assuming random heights but neglecting vertical exposure as well as another one characterized by fixed heights and capturing vertical exposure is much less computationally expensive, and both can be utilized as adequate approximations for certain ranges of system parameters.

Finally, we assessed the performance of various mmWave communication scenarios, including AP-, UAV-, and D2D-based deployments. We demonstrated that for the same intensity of communicating entities the UAV-based deployments are characterized by the best SIR conditions. It is important to note that the gains in applying UAVs instead of the standard APs are not dramatic, since the impact of heights on the SIR levels is most prominent for smaller values. Conversely, the D2D-based scenario is susceptible to the worst SIR performance.

Appendix A
Evaluating Vertical Exposure Probability

Numerical evaluation of the vertical exposure probability is the most computationally expensive component of the proposed model. Below, we briefly outline a computational procedure for estimating the vertical exposure probability $p_V(r)$.

An example of jpdf $f_{\gamma,\theta,\beta}(y_1, y_4, y_6)$ is shown in Fig. 9(a). To estimate $p_V(r)$, one needs to integrate it according to (32). Fig. 9(b) depicts regions, where $|\theta-\gamma| < \alpha_{T,V}/2 \cap |\theta-\beta| < \alpha_{R,V}/2$, over which the jpdf needs to be integrated to estimate the vertical exposure probability. Finally, the intersections between the piecewise integrand and the integration regions are given in Fig. 9(c).

To illustrate the integration process, let us fix $\theta = -\pi/3$. Fig. 10(a) displays the jpdf of $\{\gamma, \beta\}$ where $\theta = -\pi/3$. Further, by fixing $\beta = -\pi/5$, we arrive at the regions where the jpdf has different shapes of piecewise function overlapping with the $|\theta-\gamma| < \alpha_{T,V}/2 \cap |\theta-\beta| < \alpha_{R,V}/2$ as shown in Fig. 10(b). Further, we need to integrate over these regions. We obtain $p_V(r)$ in the closed form (see in (58)) by selecting one of them as shown in Fig. 10(c) to illustrate the process.

Appendix B
Propositions for Special Cases of the Model

In this Appendix, we summarize our results for the special cases of the model: (i) vertical exposure probability for omnidirectional Rx nodes, (ii) vertical exposure probability for fixed heights of communicating entities, and (iii) blockage probability for fixed heights of Tx and Rx nodes.

Proposition 5 (Vertical Exposure Probability for Omnidirectional Rx Nodes)**.** *The vertical exposure probability, $p_V(r)$, for directional antennas at Tx nodes and omnidirectional ones at Rx nodes, is established by integrating the jpdf of angles β, θ over $|\beta-\theta| < \alpha_{T,V}/2$ (Fig. 11), i.e.,*

$$p_V(r) = \int_{-\frac{\pi}{2}}^{\frac{\pi}{2}} \int_{y_4-\frac{\alpha_{T,V}}{2}}^{y_4+\frac{\alpha_{T,V}}{2}} f_{\beta,\theta}(y_1, y_4) dy_1 dy_4, \qquad (59)$$

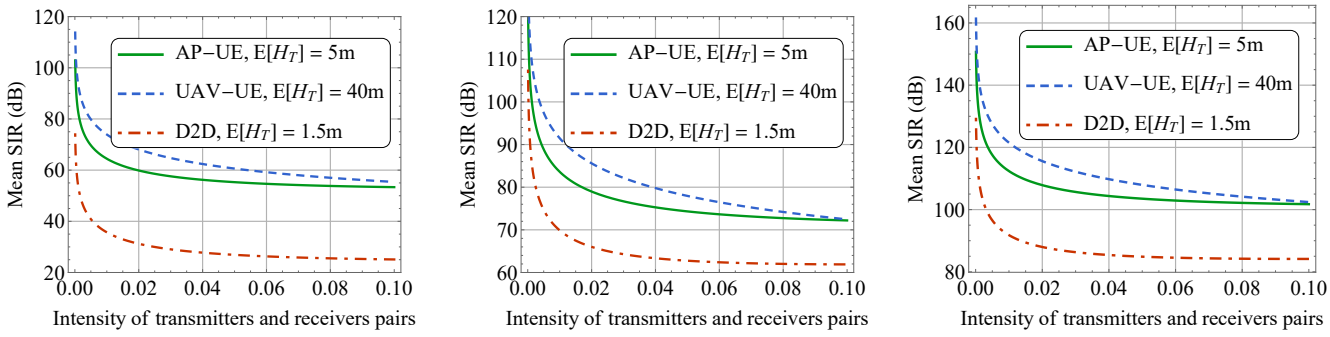

(a) Today, 128×4 Tx, 4×4 Rx (b) Near future, 128×128Tx, 4×4 Rx (c) Distant future, 128×128Tx, 64×64 Rx

Fig. 8. SIR levels for different scenarios and antenna directivities.

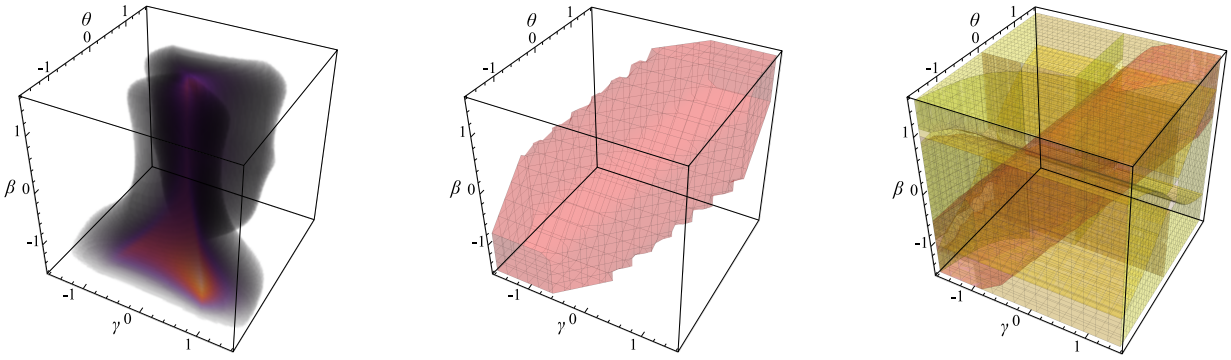

(a) Example of jpdf of $\{\gamma, \theta, \beta\}$ (b) Integration regions (c) Regions intersecting domains

Fig. 9. Details of integration for vertical exposure probability $p_V(r)$.

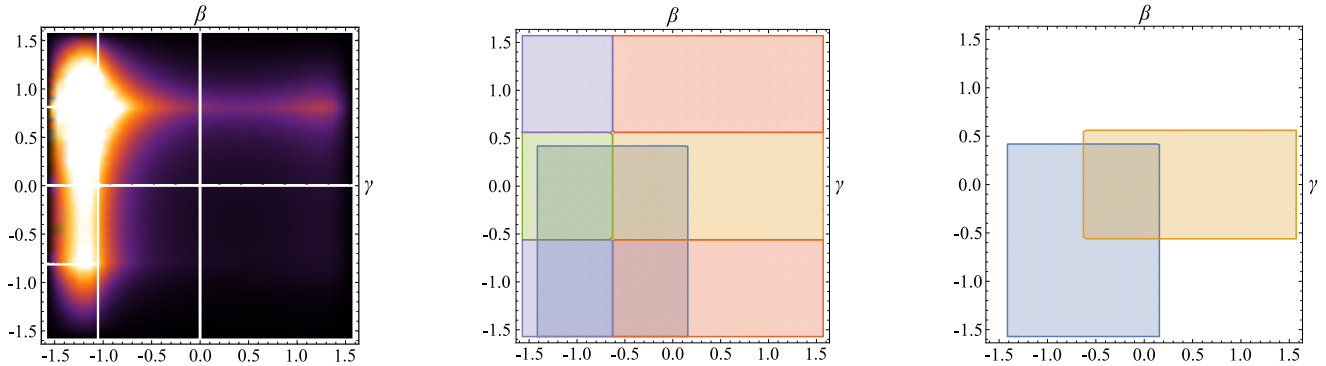

(a) jpdf, $\theta = -\pi/3$ (b) Sub-domains: $\beta = -\pi/5, \theta = -\pi/3$ (c) Region of integration

Fig. 10. Details of integration for vertical exposure probability $p_V(r)$.

where $f_{\beta,\theta}(y_1, y_4)$ *is the jpdf of* β *and* θ *is*

$$f_{\eta_1,\eta_4}(y_1, y_4) = \iiint_{\mathrm{R}^3} f_{\vec{\xi}^n}\left[\phi_i(\vec{y}^m)\right] |\mathbb{J}| dy_2 dy_3 dy_5 =$$

$$= \int_0^{R_I} \int_0^{R_T} \int_{l(y_i)}^{\infty} \frac{4\mu^3 y_3^2 y_5^2 \mathrm{e}^{-\mu(y_3 \tan(y_1) + 3y_2 + y_5 \tan(y_4))}}{\sec^{-2}(y_1) \sec^{-2}(y_4) R_I^2 R_T^2} dy_2 dy_3 dy_5 =$$

$$= \int_0^{R_I} \int_0^{R_T} \frac{4\mu^2 y_3^2 y_5^2 e^{-\mu(3l(y_i) + y_3 \tan(y_1) + y_5 \tan(y_4))}}{\sec^{-2}(y_1) \sec^{-2}(y_4) 3 R_I^2 R_T^2} dy_3 dy_5 =$$

$$= \int_0^{R_I} f_{\eta_1\eta_4\eta_5}(y_1, y_4, y_5) dy_5. \tag{60}$$

Proof. Let $\vec{\xi}^n = \{\xi_1, \ldots, \xi_4\} = \{H_R, H_T, d_T, H_{IT}\}$ and observe that its jpdf has a multiplicative form due to independence of the involved components, i.e.,

$$f_{\vec{\xi}^n}(\vec{x}^n) = \frac{2x_3}{R_T^2} \mu_R e^{-\mu_R x_1} \mu_T e^{-\mu_T x_2} \mu_T e^{-\mu_T x_4}. \tag{61}$$

Let also $\vec{\eta}^m = \{\eta_1, \eta_4\} = \{\beta, \theta\}$. Since the number of the target RVs, m, is lower than the number of the input RVs, n, we complement the target RVs with the auxiliary ones as

$$\vec{\eta}^n = \{\eta_1, \ldots, \eta_4\} = \{\beta, H_T, d_T, \theta\}. \tag{62}$$

$$p_V(r) = \int_{-\cot^{-1}\left(\frac{5\sqrt{RT^2}}{\pi}\right)}^{\frac{1}{10}(5\alpha R-2\pi)} \int_{-\tan^{-1}\left(\frac{\sqrt{5-2\sqrt{5}}r}{R_T}\right)}^{\frac{1}{10}(5\alpha_{T,V}-2\pi)} \left[\begin{array}{l} \frac{4\left(\sqrt{5}-1\right)^2 r\csc(y_1)\sec(y_1)\cot(y_6)\csc^2(y_6)e^{\frac{\pi\mu_R}{5}-\sqrt{5-2\sqrt{5}}r(\mu_R+\mu_T)-\mu_T R_T\tan(y_1)}}{\mu_R\mu_T {R_T}^4(\mu_R+2\mu_T)} \\ \times\left(e^{\mu_R R_T\tan(y_6)}(\mu_R R_T\tan(y_6)(\mu_R R_T\tan(y_6)-2)+2)-2\right) \\ \times\left({\mu_T}^2\left(-{R_T}^2\right)-2\mu_T R_T\cot(y_1)+2\cot^2(y_1)\left(e^{\mu_T R_T\tan(y_1)}-1\right)\right) \end{array}\right] dy_1 dy_6 =$$

$$= \int_{-\cot^{-1}\left(\frac{5\sqrt{R_T^2}}{\pi}\right)}^{\frac{1}{10}(5\alpha R-2\pi)} \left(\begin{array}{l} \frac{1}{\mu_R\mu_T R_T^4(\mu_R+2\mu_T)}4\left(\sqrt{5}-1\right)^2 r\cot\left(y_6\right)\csc^2\left(y_6\right) \\ \times\left(e^{\mu_R R_T\tan(y_6)}\left(\mu_R R_T\tan\left(y_6\right)\left(\mu_R R_T\tan\left(y_6\right)-2\right)+2\right)-2\right) \\ \times\left(\begin{array}{l} -\frac{\left(2\sqrt{5}+5\right)\left(\left(2\sqrt{5}-5\right)r^2-R_T^2\right)e^{\frac{\pi\mu_R}{5}-\sqrt{5-2\sqrt{5}}r(\mu_R+\mu_T)}}{10r^2} \\ \times\left(\begin{array}{l} -e^{\sqrt{5-2\sqrt{5}}\mu_T r}+\mu_T R_T e^{\sqrt{5-2\sqrt{5}}\mu_T r}\sin\left(2\tan^{-1}\left(\frac{\sqrt{5-2\sqrt{5}}r}{R_T}\right)\right) \\ -e^{\sqrt{5-2\sqrt{5}}\mu_T r}\cos\left(2\tan^{-1}\left(\frac{\sqrt{5-2\sqrt{5}}r}{R_T}\right)\right)+2 \end{array}\right) \\ -\left(\begin{array}{l} e^{\mu_T R_T\tan\left(\frac{\pi}{5}-\frac{\alpha_{T,V}}{2}\right)}+\sin\left(\alpha_{T,V}+\frac{\pi}{10}\right)e^{\mu_T R_T\tan\left(\frac{\pi}{5}-\frac{\alpha T}{2}\right)} \\ +\mu_T R_T\cos\left(\alpha T+\frac{\pi}{10}\right)\left(-e^{\mu_T R_T\tan\left(\frac{\pi}{5}-\frac{\alpha_{T,V}}{2}\right)}\right)-2 \end{array}\right)\frac{e^{\frac{\pi\mu_R}{5}-\sqrt{5-2\sqrt{5}}r(\mu_R+\mu_T)}}{\sin\left(\alpha_{T,V}+\frac{\pi}{10}\right)-1} \end{array}\right) \end{array}\right) dy_6 =$$

$$= \begin{array}{l} \frac{1}{5R_T^4\mu_R\mu_T(\mu_R+2\mu_T)}2\left(6-2\sqrt{5}\right)e^{\frac{\pi\mu_R}{5}-\sqrt{5-2\sqrt{5}}r(\mu_R+\mu_T)}r \\ \times\left(\begin{array}{l} \frac{2\left(5+2\sqrt{5}\right)\left(5r^2-2\sqrt{5}r^2+R_T^2+e^{\sqrt{5-2\sqrt{5}}r\mu_T}R_T^2\left(-1+\sqrt{5-2\sqrt{5}}r\mu_T\right)\right)}{r^2} \\ +\frac{20+10e^{R_T\mu_T\tan\left[\frac{\pi}{5}-\frac{\alpha_T}{2}\right]}\left(-1+R_T\mu_T\cos\left[\frac{\pi}{10}+\alpha_T\right]-\sin\left[\frac{\pi}{10}+\alpha_T\right]\right)}{\sin\left[\frac{\pi}{10}+\alpha_T\right]-1} \end{array}\right) \\ \times\left(\begin{array}{l} \frac{e^{-\frac{\pi\mu_R}{5}}\left(-e^{\frac{\pi\mu_R}{5}}\left(\pi^2+25R_T^2\right)+5R_T^2(5+\pi\mu_R)\right)}{\pi^2} \\ +\csc\left[\frac{\pi}{5}-\frac{\alpha_R}{2}\right]^2-e^{-R_T\mu_R\tan\left[\frac{\pi}{5}-\frac{\alpha_R}{2}\right]}\left(1+R_T\mu_R\tan\left[\frac{\pi}{5}-\frac{\alpha_R}{2}\right]\right)\tan\left[\frac{1}{10}\left(3\pi+5\alpha_R\right)\right]^2 \end{array}\right). \end{array} \tag{58}$$

$$f_{\beta,\theta}(y_1,y_4) = \begin{cases} \frac{-4r\cot(y_1)\csc^2(y_1)\sec^2(y_4)[1-e^{R_T\mu\tan(y_1)}+2R_T\mu\tan(y_1)+RT^2\mu^2\tan^2(y_1)]}{3R_T^2\mu e^{\mu[R_T\tan(y_1)+r\tan[y_4]]}}, & y_1\geq 0\cap y_4\geq 0, \\ \frac{4r\cot(y_1)\csc^2(y_1)\sec^2(y_4)[e^{R_T\mu\tan(y_1)}-2R_T\mu\tan(y_1)-R_T^2\mu^2\tan^2(y_1)-1]}{3RT^2\mu e^{R_T\mu\tan(y_1)+2r\mu\tan(y_4)}}, & \\ & y_4<0\cap\left(R_T\tan y_1\geq r\tan y_4\cup y_1\geq 0\right), \\ \frac{2e^{2R_T\mu\tan(y_1)}RT^2\mu^2-2e^{2R_T\mu\tan(y_1)}R_T\mu\cot(y_1)-\cot^2(y_1)+e^{2R_T\mu\tan(y_1)}\cot^2(y_1)}{6r^{-1}\csc^{-1}(y_1)\sec^{-1}(y_1)\sec^{-12}(y_4)R_T^2\mu e^{r\mu\tan(y_4)}}, & y_1<0\cap y_4\geq 0, \\ \frac{r\cot(y_1)\csc(y_1)\sec^2(y_4)}{6R_T^2\mu e^{r\mu\tan(y_4)}}\times & \\ \left(e^{2R_T\mu\tan(y_1)}\csc(y_1)-9e^{2r\mu\tan(y_4)}\csc(y_1)+8e^{3r\mu\tan(y_4)}\csc(y_1)-\right. & \\ -2e^{2R_T\mu\tan(y_1)}R_T\mu\sec(y_1)+2e^{2R_T\mu\tan(y_1)}R_T^2\mu^2\sec(y_1)\tan(y_1)- & \text{elsewhere.} \\ \left.-6e^{2r\mu\tan(y_4)}r\mu\csc(y_1)\tan(y_4)-6e^{2r\mu\tan(y_4)}r^2\mu^2\csc(y_1)\tan^2(y_4)\right), & \end{cases} \tag{66}$$

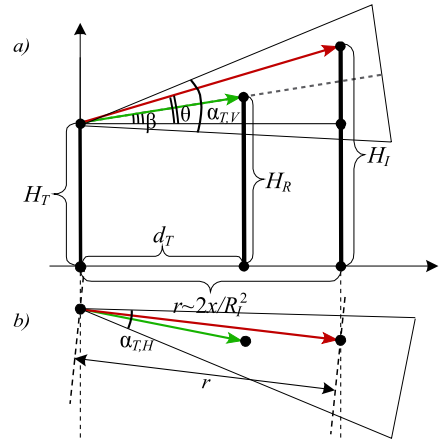

Fig. 11. Vertical exposure for omnidirectional Rx nodes.

Hence, the transformation in question is

$$\begin{cases} y_1 = f_1(\vec{x}^n) = \beta = \arctan[(x_1-x_2)/x_3] \\ y_4 = f_4(\vec{x}^n) = \theta = \arctan[(x_4-x_2)/r] \end{cases}, \tag{63}$$

and the auxiliary functions are $f_i(\vec{x}^n) = x_i$, $i=\{2,3\}$.

The inverses are bijections in the domains of interest, i.e.,

$$\begin{cases} x_1 = \phi_1(\vec{y}^n) = y_2 + y_3\tan y_1 \\ x_4 = \phi_4(\vec{y}^n) = y_2 + r\tan y_4 \end{cases}, \tag{64}$$

which are complemented with $x_i = \phi_i(\vec{y}^n) = y_i$, $i=\{2,3\}$.

The jpdf can then be represented as

$$f_{\vec{\eta}^n}(\vec{y}^n) = f_{\xi^n}(\phi_1(\vec{y}^n),\ldots,\phi_n(\vec{y}^n))|\mathbb{J}|, \tag{65}$$

where the Jacobian of the transformation is computed in the form of $\mathbb{J} = y_3 r\sec^2 y_1\sec^2 y_4$ and the jpdf $f_{\vec{\xi}^n}(\phi_1(\vec{y}^n),\ldots,\phi_n(\vec{y}^n))$ takes the form of (61).

Denoting $l(y_i) = \max(0, -y_3 \tan y_1, -r \tan y_4)$, we obtain (60). Performing the last integration, we arrive at the jpdf of β and θ, $f_{\beta,\theta}(y_1, y_4)$ as in (66).

□

Proposition 6 (Vertical Exposure Probability for Fixed Heights of Tx and Rx)**.** *The vertical exposure probability for fixed heights of Tx and Rx nodes, h_T and h_R, is given by*

$$p_V(r) = p_V(r, \alpha_{T,V}) p_V(r, \alpha_{R,V}), \tag{67}$$

where the probability $p_V(r, \alpha)$ is

$$\begin{cases} \frac{(h_T - h_R)^2 \left[\cot\left(\frac{\alpha}{2} - \gamma\right)^2 - \cot\left(\frac{\alpha}{2} + \gamma\right)^2\right]}{R_T^2}, & (h_T - h_R) r \in U_1, \\ \frac{1 - (h_T - h_R)^2 \cot\left(\frac{\alpha}{2} + \gamma\right)^2}{R_T^2}, & (h_T - h_R) r \in U_2, \end{cases} \tag{68}$$

where the regions are determined by

$$U_1 = (A_+, B) \cup (B, A_+),\ U_2 = (A_+, A_-) \cup (A_-, B), \tag{69}$$

and $A_\pm = \cot(\pm\alpha/2 + \gamma_0)$, $B = \cot([\pi - \alpha]/2)$.

Proof. Observe that when the heights of Tx and Rx nodes are constant, the angles θ, γ, and β are mutually independent, see Fig. 11. Therefore, the vertical exposure probability $p_V(r)$ can be written as $p_V(r) = p_V(r, \alpha_{T,V}) p_V(r, \alpha_{R,V})$, where $p_V(r, \alpha_{T,V})$ and $p_V(r, \alpha_{R,V})$ are the probabilities that Tx 'hits' a non-tagged Rx and the antenna of the Rx is directed towards a non-tagged Tx, respectively. These probabilities can be established similarly as follows.

Let ξ be the distance between Tx and Rx, and α be the antenna directivity. Denoting the sought angle by ϵ, we have

$$p_V(r, \alpha) = \int_{\gamma - \alpha/2}^{\gamma + \alpha/2} f_\epsilon(x) dx, \tag{70}$$

where $f_\epsilon(x)$ is the pdf of the RV ϵ.

The transformation of interest is $\phi(y) = (h_T - h_R)\cot(y)$ and the pdf is $f_\xi(x) = 2R_T^{-2} x$. Completing the said transformation, we obtain $f_\epsilon(y)$ in the following form

$$f_\epsilon(y) = \frac{2(h_T - h_R)^2 \cot(y) \csc(y^2)}{R_T^2},\ 0 < y < \frac{\pi}{2}. \tag{71}$$

Performing the integration, we arrive at (68). □

Proposition 7 (Blockage Probability for Fixed Heights of Tx and Rx)**.** *The blockage probability in a Poisson field of blockers with fixed heights of Tx and Rx, h_T and h_R, is*

$$p_B(r) = 1 - e^{\frac{2\lambda\left(e^{-h_R\mu_B} - e^{-h_T\mu_B}\right) r_B r}{(h_R - h_T)\mu_B}}. \tag{72}$$

Proof. Assuming $h_T > h_R$, observe that the height of the LoS path is uniformly distributed within (h_R, h_T). Since the pdf of the difference between the LoS path and the height of a blocker is uniformly distributed in $(0, R_I)$, G_r is a convolution of the uniform and the exponential distributions, i.e.,

$$f_{G_r}(y) = \frac{e^{-(h_R + h_T - y)\mu_B}\left(e^{h_R\mu_B} - e^{h_T\mu_B}\right)}{h_R - h_T} - \\ - \frac{-1 + e^{(-h_T + y)\mu_B}}{h_T - h_R},\ h_R < y \cap h_T > y. \tag{73}$$

Then, the probability of blockage by a single obstacle is

$$p_{B,1}(r) = 1 - Pr\{G_r > 0\} = 1 - \int_0^\infty f_{G_r}(y) dy = \\ 1 - \frac{e^{-h_R\mu_B} - e^{-h_T\mu_B} + h_R\mu_B - h_T\mu_B}{h_R\mu_B - h_T\mu_B} = \\ = \frac{-e^{-h_R\mu_B} + e^{-h_T\mu_B}}{(h_R - h_T)\,\mu_B}. \tag{74}$$

Substituting (74) into (20), we arrive at (72). □

REFERENCES

[1] Cisco, "Global mobile data traffic forecast 2016–2021," White Paper, 2017.

[2] G. George and A. Lozano, "Impact of reflections in enclosed mmWave wearable networks," in *Proc. of 6th International Workshop on Computational Advances in Multi-Sensor Adaptive Processing (CAMSAP)*. IEEE, 2015, pp. 201–204.

[3] K. Venugopal and R. W. Heath, "Location based performance model for indoor mmWave wearable communication," in *Proc. of International Conference on Communications (ICC)*. IEEE, 2016, pp. 1–6.

[4] Y. Wang and Z. Shi, "Millimeter-Wave Mobile Communications," in *5G Mobile Communications*. Springer, 2017, pp. 117–134.

[5] J. G. Andrews, S. Buzzi, W. Choi, S. V. Hanly, A. Lozano, A. C. Soong, and J. C. Zhang, "What will 5G be?" *IEEE Journal on Selected Areas in Communications*, vol. 32, no. 6, pp. 1065–1082, 2014.

[6] M. Gapeyenko, A. Samuylov, M. Gerasimenko, D. Moltchanov, S. Singh, E. Aryafar, S.-p. Yeh, N. Himayat, S. Andreev, and Y. Koucheryavy, "Analysis of human-body blockage in urban millimeter-wave cellular communications," in *Proc. of International Conference on Communications (ICC)*. IEEE, 2016, pp. 1–7.

[7] A. Orsino, A. Ometov, G. Fodor, D. Moltchanov, L. Militano, S. Andreev, O. N. Yilmaz, T. Tirronen, J. Torsner, G. Araniti *et al.*, "Effects of heterogeneous mobility on D2D-and drone-assisted mission-critical MTC in 5G," *IEEE Communications Magazine*, vol. 55, no. 2, pp. 79–87, 2017.

[8] Y. Orlov, E. Kirina-Lilinskaya, A. Samuylov, A. Ometov, D. Moltchanov, Y. Gaimamaka, S. Andreev, and K. Samouylov, "Time-Dependent SIR Analysis in Shopping Malls Using Fractal-Based Mobility Models," in *Proc. of International Conference on Wired/Wireless Internet Communication*. Springer, 2017, pp. 16–25.

[9] S. N. Chiu, D. Stoyan, W. S. Kendall, and J. Mecke, *Stochastic geometry and its applications*. John Wiley & Sons, 2013.

[10] V. Petrov, D. Moltchanov, and Y. Koucheryavy, "On the efficiency of spatial channel reuse in ultra-dense THz networks," in *Proc. of IEEE Globecom*, Dec. 2015.

[11] V. Petrov, M. Komarov, D. Moltchanov, J. M. Jornet, and Y. Koucheryavy, "Interference and SINR in Millimeter Wave and Terahertz Communication Systems With Blocking and Directional Antennas," *IEEE Transactions on Wireless Communications*, vol. 16, no. 3, pp. 1791–1808, 2017.

[12] M. Di Renzo, "Stochastic geometry modeling and analysis of multi-tier millimeter wave cellular networks," *IEEE Transactions on Wireless Communications*, vol. 14, no. 9, pp. 5038–5057, 2015.

[13] K. Venugopal and R. Heath, "Millimeter Wave Networked Wearables in Dense Indoor Environments," *IEEE Access*, vol. 4, pp. 1205–1221, Apr. 2016.

[14] S. Singh, M. N. Kulkarni, A. Ghosh, and J. G. Andrews, "Tractable model for rate in self-backhauled millimeter wave cellular networks," *IEEE Journal on Selected Areas in Communications*, vol. 33, no. 10, pp. 2196–2211, 2015.

[15] D. Moltchanov, P. Kustarev, and Y. Koucheryavy, "Analytical approximations for interference and SIR densities in terahertz systems with atmospheric absorption, directional antennas and blocking," *Physical Communication*, vol. 26, pp. 21–30, 2018.

[16] V. Petrov, D. Solomitckii, A. Samuylov, M. A. Lema, M. Gapeyenko, D. Moltchanov, S. Andreev, V. Naumov, K. Samouylov, M. Dohler *et al.*, "Dynamic Multi-Connectivity Performance in Ultra-Dense Urban mmWave Deployments," *IEEE Journal on Selected Areas in Communications*, vol. 35, no. 9, pp. 2038–2055, 2017.

[17] M. Polese, M. Giordani, M. Mezzavilla, S. Rangan, and M. Zorzi, "Improved handover through dual connectivity in 5G mmWave mobile networks," *IEEE Journal on Selected Areas in Communications*, vol. 35, no. 9, pp. 2069–2084, 2017.

[18] H. Park, S. Park, T. Song, and S. Pack, "An incremental multicast grouping scheme for mmWave networks with directional antennas," *IEEE Communications Letters*, vol. 17, no. 3, pp. 616–619, 2013.

[19] R.-Y. Chao, K. Fujimoto, and K. Hirasawa, "Three-dimensional performance of an LMS adaptive array with inverted-F elements," *IEEE Transactions on Vehicular Technology*, vol. 40, no. 3, pp. 575–583, 1991.

[20] J. Nasreddine, J. Riihijärvi, A. Achtzehn, and P. Mähönen, "The World is not flat: Wireless communications in 3D environments," in *Proc. of 14th International Symposium and Workshops on a World of Wireless, Mobile and Multimedia Networks (WoWMoM)*. IEEE, 2013, pp. 1–9.

[21] F. Letourneux, Y. Corre, E. Suteau, and Y. Lostanlen, "3D coverage analysis of LTE urban heterogeneous networks with dense femtocell deployments," *Journal on Wireless Communications and Networking*, vol. 2012, no. 1, p. 319, 2012.

[22] A. Müller, J. Hoydis, R. Couillet *et al.*, "Optimal 3D cell planning: A random matrix approach," in *Proc. of Global Communications Conference (GLOBECOM)*. IEEE, 2012, pp. 4512–4517.

[23] M. Kaur and A. Trivedi, "A 3D model analysis of mmWave wearable networks," in *Proc. of Conference on Information and Communication Technology (CICT)*. IEEE, 2017, pp. 1–6.

[24] A. Kammoun, M. Debbah, M.-S. Alouini *et al.*, "3D massive MIMO systems: Modeling and performance analysis," *IEEE Transactions on Wireless Communications*, vol. 14, no. 12, pp. 6926–6939, 2015.

[25] A. K. Gupta, X. Zhang, and J. G. Andrews, "SINR and throughput scaling in ultradense urban cellular networks," *IEEE Wireless Communications Letters*, vol. 4, no. 6, pp. 605–608, 2015.

[26] J.-M. Kelif and M. Coupechoux, "A 3D Spatial Fluid Model for Wireless Networks," *arXiv preprint arXiv:1604.04457*, 2016.

[27] M. Dong, W.-M. Chan, T. Kim, K. Liu, H. Huang, and G. Wang, "Simulation study on millimeter wave 3D beamforming systems in urban outdoor multi-cell scenarios using 3D ray tracing," in *Proc. of 26th Annual International Symposium on Personal, Indoor, and Mobile Radio Communications (PIMRC)*. IEEE, 2015, pp. 2265–2270.

[28] V. Semkin, D. Solomitckii, R. Naderpour, S. Andreev, Y. Koucheryavy, and A. V. Räisänen, "Characterization of radio links at 60 GHz using simple geometrical and highly accurate 3-D models," *IEEE Transactions on Vehicular Technology*, vol. 66, no. 6, pp. 4647–4656, 2017.

[29] V. Degli-Esposti, F. Fuschini, E. M. Vitucci, M. Barbiroli, M. Zoli, L. Tian, X. Yin, D. A. Dupleich, R. Müller, C. Schneider *et al.*, "Ray-tracing-based mm-Wave beamforming assessment," *IEEE Access*, vol. 2, pp. 1314–1325, 2014.

[30] S. G. Larew, T. A. Thomas, M. Cudak, and A. Ghosh, "Air interface design and ray tracing study for 5G millimeter wave communications," in *Proc. of Globecom Workshops (GC Wkshps)*. IEEE, 2013, pp. 117–122.

[31] D. Kovalchukov, R Moltchanov, A. Samuilov, A. Ometov, S. Andreev, Y. Koucheryavy, and K. Samuilov, "Modeling Three-Dimensional Interference and SIR in Highly Directional mmWave Communications," in *Proc. of IEEE Global Communications Conference (GLOBECOM)*. IEEE, 2017, pp. 1–7.

[32] S. Singh, R. Mudumbai, and U. Madhow, "Interference Analysis for Highly Directional 60-GHz Mesh Networks: The Case for Rethinking Medium Access Control," *IEEE/ACM Transactions on Networking*, vol. 19, no. 5, pp. 1513–1527, Oct 2011.

[33] M. Petrera and Y. B. Suris, "Spherical geometry and integrable systems," *Geometriae Dedicata*, vol. 169, no. 1, pp. 83–98, Apr 2014. [Online]. Available: https://doi.org/10.1007/s10711-013-9843-4

[34] 3GPP, "Study on channel model for frequencies from 0.5 to 100 GHz (Release 14)," 3GPP TR 38.901 V14.1.1, July 2017.

[35] J. G. Andrews, R. K. Ganti, M. Haenggi, N. Jindal, and S. Weber, "A primer on spatial modeling and analysis in wireless networks," *IEEE Communications Magazine*, vol. 48, no. 11, 2010.

[36] M. Haenggi, *Stochastic geometry for wireless networks*. Cambridge University Press, 2012.

[37] M. G. Kendall *et al.*, *The Advanced Theory of Statistics*. Charles Griffin and Co., Ltd., 42 Drury Lane, London, 1948, vol. 1, Ed. 4.

[38] S. Chiu, D. Stoyan, W. Kendall, and J. Mecke, *Stochastic geometry and its applications*. Wiley, 2013.

[39] S. Ross, *Introduction to probability models*. Academic Press, 2010.

[40] M. Abramowitz and I. Stegun, *Handbook of Mathematical Functions with Formulas, Graphs, and Mathematical Tables*. Dover, 1965.

[41] T. A. Thomas, H. C. Nguyen, G. R. MacCartney, and T. S. Rappaport, "3D mmWave Channel Model Proposal," in *Proc. of 80th Vehicular Technology Conference (VTC2014-Fall)*, September 2014, pp. 1–6.

[42] P. Massart, "Concentration inequalities and model selection," 2007.

[43] V. Va, J. Choi, and R. Heath, "The impact of beamwidth on temporal channel variation in vehicular channels and its implications," *IEEE Transactions on Vehicular Technology*, 2016.

[44] S. Hur, T. Kim, D. J. Love, J. V. Krogmeier, T. A. Thomas, A. Ghosh *et al.*, "Millimeter wave beamforming for wireless backhaul and access in small cell networks." *IEEE Trans. Communications*, vol. 61, no. 10, pp. 4391–4403, 2013.

[45] A. B. Constantine and et. al., "Antenna theory: Analysis and design," *Microstrip Antennas (third edition), John Wiley & Sons*, 2005.

Supplement A Joint probability density function $f_{\gamma,\theta,\beta}(y_1, y_4, y_6)$

$$
\begin{cases}
\frac{1}{(\mu_R R_T^4(\mu_R+\mu_T)^3(\mu_R+2\mu_T))}\left(\begin{array}{l} 4\mu_T^2 r\csc(y_1)\sec(y_1)\sec^2(y_4)\cot(y_6)\csc^2(y_6)\left(e^{\mu_R R_T\tan(y_6)}(\mu_R R_T\tan(y_6)(\mu_R R_T\tan(y_6)-2)+2)-2\right)\times \\ \times e^{\mu_R(-y_4)-\mu_T r\tan(y_4)}\left(e^{R_T(\mu_R+\mu_T)\tan(y_1)}\left(R_T^2(\mu_R+\mu_T)^2+2\cot(y_1)(\cot(y_1)-R_T(\mu_R+\mu_T))\right)-2\cot^2(y_1)\right)\end{array}\right)- \\
-\frac{4r\cot(y_1)\csc^2(y_6)}{\mu_R\mu_T R_T^4(\mu_R+2\mu_T)}\csc^2(y_1)\sec^2(y_4)\cot(y_6)\left(\mu_T R_T\tan(y_1)(\mu_T R_T\tan(y_1)+2)-2e^{\mu_T R_T\tan(y_1)}+2\right)\times \\
\times\left(e^{\mu_R R_T\tan(y_6)}(\mu_R R_T\tan(y_6)(\mu_R R_T\tan(y_6)-2)+2)-2\right)e^{\mu_R(-y_4)-\mu_T(R_T\tan(y_1)+r\tan(y_4))} \\
\\
\frac{4r\csc(y_1)\sec(y_1)}{\mu_R\mu_T R_T^4(\mu_R+2\mu_T)}\sec^2(y_4)\cot(y_6)\csc^2(y_6)\times\left(e^{\mu_R R_T\tan(y_6)}(\mu_R R_T\tan(y_6)(\mu_R R_T\tan(y_6)-2)+2)-2\right)\times \\
\times\left(\mu_T^2\left(-R_T^2\right)-2\mu_T R_T\cot(y_1)+2\cot^2(y_1)\left(e^{\mu_T R_T\tan(y_1)}-1\right)\right)e\left(-\mu_T R_T\tan(y_1)+r(\mu_R+\mu_T)\tan(y_4)+\mu_R(-y_4)\right) \\
\\
-\frac{4r\cot(y_1)\csc^2(y_1)}{\mu_R\mu_T R_T^4(\mu_R+2\mu_T)}\sec^2(y_4)\cot(y_6)\csc^2(y_6)\left(\mu_T R_T\tan(y_1)(\mu_T R_T\tan(y_1)+2)-2e^{\mu_T R_T\tan(y_1)}+2\right)\times \\
\times\left(e^{\mu_R R_T\tan(y_6)}(\mu_R R_T\tan(y_6)(\mu_R R_T\tan(y_6)-2)+2)-2\right)\left(e^{r(\mu_R+2\mu_T)\tan(y_4)}+1\right)e^{\mu_R(-y_4)-\mu_T(R_T\tan(y_1)+r\tan(y_4))}\times \\
\times\frac{4r\cot(y_1)\csc^2(y_1)\sec^2(y_4)}{\mu_R\mu_T R_T^4(\mu_R+\mu_T)^3(\mu_R+2\mu_T)}\cot(y_6)\csc^2(y_6)\left(e^{\mu_R R_T\tan(y_6)}(\mu_R R_T\tan(y_6)(\mu_R R_T\tan(y_6)-2)+2)-2\right)e^{\mu_R(-y_4)-\mu_T(R_T\tan(y_1)+r\tan(y_4))}\times \\
\times\left(\begin{array}{l} 2\left((\mu_R+\mu_T)^3\left(e^{\mu_T R_T\tan(y_1)}-1\right)e^{r(\mu_R+2\mu_T)\tan(y_4)}+\mu_T^3 e^{\mu_T R_T\tan(y_1)}\left(e^{R_T(\mu_R+\mu_T)\tan(y_1)}-1\right)\right)+\mu_T R_T(\mu_R+\mu_T)\tan(y_1)\times \\ \times\left(\mu_T^2 e^{R_T(\mu_R+2\mu_T)\tan(y_1)}(R_T(\mu_R+\mu_T)\tan(y_1)-2)-(\mu_R+\mu_T)^2(\mu_T R_T\tan(y_1)+2)e^{r(\mu_R+2\mu_T)\tan(y_4)}\right)\end{array}\right) \\
-\frac{4r\cot(y_1)\csc^2(y_1)}{\mu_R\mu_T R_T^4(\mu_R+2\mu_T)}\sec^2(y_4)\cot(y_6)\csc^2(y_6)\left(e^{\mu_R R_T\tan(y_6)}(\mu_R R_T\tan(y_6)(\mu_R R_T\tan(y_6)-2)+2)-2\right)\times \\
\times e^{\mu_R r\tan(y_4)-\mu_R y_4}\left(\mu_T r\tan(y_4)(\mu_T r\tan(y_4)+2)-2e^{\mu_T r\tan(y_4)}+2\right) \\
-\frac{4r\cot(y_1)\sec^2(y_4)}{\mu_R\mu_T R_T^4(\mu_R+\mu_T)^3(\mu_R+2\mu_T)}\cot(y_6)\csc^2(y_6)\left(e^{\mu_R R_T\tan(y_6)}(\mu_R R_T\tan(y_6)(\mu_R R_T\tan(y_6)-2)+2)-2\right)e^{\mu_R(-y_4)-\mu_T r\tan(y_4)} \\
\times\left(\begin{array}{l} \mu_T^3 R_T^2(\mu_R+\mu_T)^2\sec^2(y_1)\left(-e^{R_T(\mu_R+\mu_T)\tan(y_1)}\right)+\csc^2(y_1) \\ \times\left(\begin{array}{l} -2\mu_T^3 e^{R_T(\mu_R+\mu_T)\tan(y_1)}+2(\mu_R+2\mu_T)\left(\mu_R^2+\mu_R\mu_T+\mu_T^2\right)e^{r(\mu_R+\mu_T)\tan(y_4)}+\mu_T r(\mu_R+\mu_T)(\mu_R+2\mu_T)\tan(y_4)e^{r(\mu_R+\mu_T)\tan(y_4)}\times \\ \times(2\mu_R+\mu_T r(\mu_R+\mu_T)\tan(y_4))-2(\mu_R+\mu_T)^3 e^{r(\mu_R+2\mu_T)\tan(y_4)}\end{array}\right) \\ +2\mu_T^3 R_T(\mu_R+\mu_T)\csc(y_1)\sec(y_1)e^{R_T(\mu_R+\mu_T)\tan(y_1)}\end{array}\right) \\
\frac{4\mu_T^2 r\csc(y_1)\sec(y_1)}{\mu_R R_T^4(\mu_R+\mu_T)^3(\mu_R+2\mu_T)}\sec^2(y_4)\cot(y_6)\csc^2(y_6)e^{\mu_R(-y_4)-\mu_T r\tan(y_4)}\left(\begin{array}{l} R_T^2(\mu_R+\mu_T)^2 e^{R_T(\mu_R+\mu_T)\tan(y_1)}+2\cot(y_1) \\ \times\left(e^{R_T(\mu_R+\mu_T)\tan(y_1)}(\cot(y_1)-R_T(\mu_R+\mu_T))-\cot(y_1)\right)\end{array}\right)\times \\
\left(e^{\mu_R\tan(y_6)|y_4\cot(y_6)|}\left(\mu_R\tan(y_6)\left(\mu_R y_4^2\cot(y_6)-2\left|y_4\cot(y_6)\right|\right)+2\right)-2\right) \\
-\frac{4r\cot(y_1)\csc^2(y_1)}{\mu_R\mu_T R_T^4(\mu_R+2\mu_T)}\sec^2(y_4)\csc^2(y_6)\left(\mu_T R_T\tan(y_1)(\mu_T R_T\tan(y_1)+2)-2e^{\mu_T R_T\tan(y_1)}+2\right)\times \\
\times\left(\left(-2\mu_R\left|y_4\cot(y_6)\right|+\mu_R^2 y_4^2\cot(y_6)+2\cot(y_6)\right)e^{\mu_R\tan(y_6)|y_4\cot(y_6)|}-2\cot(y_6)\right)e^{\mu_R(-y_4)-\mu_T(R_T\tan(y_1)+r\tan(y_4))} \\
\frac{4r\cot(y_1)\csc^2(y_1)}{\mu_R\mu_T R_T^4(\mu_R+2\mu_T)}\sec^2(y_4)\csc^2(y_6)\left(2\left(e^{\mu_T R_T\tan(y_1)}-1\right)-\mu_T R_T\tan(y_1)(\mu_T R_T\tan(y_1)+2)\right)\times \\
\times\left(\left(-2\mu_R\left|y_4\cot(y_6)\right|+\mu_R^2 y_4^2\cot(y_6)+2\cot(y_6)\right)e^{\mu_R\tan(y_6)|y_4\cot(y_6)|}-2\cot(y_6)\right)e\left(-\mu_T R_T\tan(y_1)+r(\mu_R+\mu_T)\tan(y_4)+\mu_R(-y_4)\right) \\
-\frac{4r\cot(y_1)\csc^2(y_1)}{\mu_R\mu_T R_T^4(\mu_R+2\mu_T)}\sec^2(y_4)\csc^2(y_6)\left(\mu_T R_T\tan(y_1)(\mu_T R_T\tan(y_1)+2)-2e^{\mu_T R_T\tan(y_1)}+2\right)\left(e^{r(\mu_R+2\mu_T)\tan(y_4)}+1\right)\times \\
\times\left(\left(-2\mu_R\left|y_4\cot(y_6)\right|+\mu_R^2 y_4^2\cot(y_6)+2\cot(y_6)\right)e^{\mu_R\tan(y_6)|y_4\cot(y_6)|}-2\cot(y_6)\right)e^{\mu_R(-y_4)-\mu_T(R_T\tan(y_1)+r\tan(y_4))} \\
\frac{4r\cot(y_1)\csc^2(y_1)\sec^2(y_4)}{\mu_R\mu_T R_T^4(\mu_R+\mu_T)^3(\mu_R+2\mu_T)}\cot(y_6)\csc^2(y_6)e^{\mu_R(-y_4)-\mu_T(R_T\tan(y_1)+r\tan(y_4))} \\
\times\left(e^{\mu_R\tan(y_6)|y_4\cot(y_6)|}\times\left(\mu_R\tan(y_6)\left(\mu_R y_4^2\cot(y_6)-2\left|y_4\cot(y_6)\right|\right)+2\right)-2\right)\times \\
\times\left(\begin{array}{l} 2\left((\mu_R+\mu_T)^3\left(e^{\mu_T R_T\tan(y_1)}-1\right)e^{r(\mu_R+2\mu_T)\tan(y_4)}+\mu_T^3 e^{\mu_T R_T\tan(y_1)}\left(e^{R_T(\mu_R+\mu_T)\tan(y_1)}-1\right)\right)+\mu_T R_T(\mu_R+\mu_T)\tan(y_1)\times \\ \times\left(\mu_T^2 e^{R_T(\mu_R+2\mu_T)\tan(y_1)}(R_T(\mu_R+\mu_T)\tan(y_1)-2)-(\mu_R+\mu_T)^2(\mu_T R_T\tan(y_1)+2)e^{r(\mu_R+2\mu_T)\tan(y_4)}\right)\end{array}\right) \\
-\frac{4r\cot(y_1)\csc^2(y_1)}{\mu_R\mu_T R_T^4(\mu_R+2\mu_T)}\sec^2(y_4)\cot(y_6)\csc^2(y_6)e^{\mu_R r\tan(y_4)-\mu_R y_4}\left(\mu_T r\tan(y_4)(\mu_T r\tan(y_4)+2)-2e^{\mu_T r\tan(y_4)}+2\right)\times \\
\times\left(e^{\mu_R\tan(y_6)|y_4\cot(y_6)|}\left(\mu_R\tan(y_6)\left(\mu_R y_4^2\cot(y_6)-2\left|y_4\cot(y_6)\right|\right)+2\right)-2\right) \\
\frac{4r\cot(y_1)\csc^2(y_1)\sec^2(y_4)\csc^2(y_6)}{\mu_R\mu_T R_T^4(\mu_R+\mu_T)^3(\mu_R+2\mu_T)}e^{\mu_R(-y_4)-\mu_T r\tan(y_4)}\times \\
\times\left(\mu_R\left(2\sqrt{y_4^2\cot(y_6)\cot(y_6)}-\mu_R y_4^2\cot(y_6)\right)e^{\mu_R\tan(y_6)\sqrt{y_4^2\cot(y_6)\cot(y_6)}}-2\cot(y_6)\left(e^{\mu_R\tan(y_6)\sqrt{y_4^2\cot(y_6)\cot(y_6)}}-1\right)\right)\times \\
\times\left(\begin{array}{l} \mu_T^3 R_T^2(\mu_R+\mu_T)^2\sec^2(y_1)\left(-e^{R_T(\mu_R+\mu_T)\tan(y_1)}\right)+\csc^2(y_1)\times \\ \times\left(\begin{array}{l} -2\mu_T^3 e^{R_T(\mu_R+\mu_T)\tan(y_1)}+2(\mu_R+2\mu_T)\left(\mu_R^2+\mu_R\mu_T+\mu_T^2\right)e^{r(\mu_R+\mu_T)\tan(y_4)}+\mu_T r(\mu_R+\mu_T)(\mu_R+2\mu_T)\tan(y_4)e^{r(\mu_R+\mu_T)\tan(y_4)} \\ \times(2\mu_R+\mu_T r(\mu_R+\mu_T)\tan(y_4))-2(\mu_R+\mu_T)^3 e^{r(\mu_R+2\mu_T)\tan(y_4)}\end{array}\right) \\ +2\mu_T^3 R_T(\mu_R+\mu_T)\csc(y_1)\sec(y_1)e^{R_T(\mu_R+\mu_T)\tan(y_1)}\end{array}\right)+
\end{cases}
$$

$$
\begin{cases}
\left(\begin{array}{l} R_T<\left|y_4\cot(y_6)\right|\wedge y_1<0\wedge y_4\geq 0 \\ \wedge R_T\tan(y_1)\leq r\tan(y_4)\end{array}\right)\vee\left(\begin{array}{l} R_T\leq\left|y_4\cot(y_6)\right|\wedge y_1<0\wedge y_4\geq 0 \\ \wedge R_T\tan(y_1)<r\tan(y_4)\end{array}\right) \\
\left(R_T=\left|y_4\cot(y_6)\right|\wedge y_1\geq 0\wedge y_4\geq 0\right)\vee\left(R_T\leq\left|y_4\cot(y_6)\right|\wedge y_1>0\wedge y_4\geq 0\right) \\
\vee\left(R_T\leq\left|y_4\cot(y_6)\right|\wedge y_1\geq 0\wedge y_4\geq 0\wedge R_T\tan(y_1)\leq r\tan(y_4)\right) \\
\left(R_T=\left|y_4\cot(y_6)\right|\wedge y_1\geq 0\wedge y_4<0\right)\vee\left(R_T<\left|y_4\cot(y_6)\right|\wedge y_1>0\wedge y_4<0\right)\vee \\
\vee\left(R_T=\left|y_4\cot(y_6)\right|\wedge y_4<0\wedge R_T\tan(y_1)\geq r\tan(y_4)\right)\vee \\
\vee\left(R_T\leq\left|y_4\cot(y_6)\right|\wedge y_1>0\wedge y_4<0\wedge R_T\tan(y_1)\geq r\tan(y_4)\right)\vee \\
\vee\left(R_T<\left|y_4\cot(y_6)\right|\wedge y_4<0\wedge R_T\tan(y_1)>r\tan(y_4)\right) \\
y_1=0\wedge R_T<\left|y_4\cot(y_6)\right|\wedge y_4\geq 0\wedge R_T\tan(y_1)>\tan(y_4) \\
\left(R_T=\left|y_4\cot(y_6)\right|\wedge y_1<0\wedge R_T\tan(y_1)\geq r\tan(y_4)\wedge y_4\geq 0\right)\vee \\
\vee\left(R_T<\left|y_4\cot(y_6)\right|\wedge y_1<0\wedge R_T\tan(y_1)>r\tan(y_4)\wedge y_4\geq 0\right) \\
\left(y_1=0\wedge y_4<0\wedge R_T<\left|y_4\cot(y_6)\right|\wedge R_T\tan(y_1)\leq r\tan(y_4)\right)\vee \\
\vee\left(y_1\leq 0\wedge y_4<0\wedge R_T<\left|y_4\cot(y_6)\right|\wedge R_T\tan(y_1)=r\tan(y_4)\right) \\
\left|y_4\cot(y_6)\right|\neq 0\wedge y_1<0\wedge R_T\tan(y_1)<r\tan(y_4)\wedge y_4<0\wedge R_T\leq\left|y_4\cot(y_6)\right| \\
\left(\left|y_4\cot(y_6)\right|\geq 0\wedge y_1<0\wedge R_T\tan(y_1)<r\tan(y_4)\wedge y_4\geq 0 R_T>\left|y_4\cot(y_6)\right|\right) \\
\vee\left(\left|y_4\cot(y_6)\right|>0\wedge y_1<0\wedge R_T\tan(y_1)\leq r\tan(y_4)\wedge y_4\geq 0\wedge R_T>\left|y_4\cot(y_6)\right|\right) \\
(y_4\cot(y_6)=0\wedge y_1\geq 0\wedge y_4\geq 0\wedge R_T>y_4\cot(y_6)) \\
\vee(y_4\cot(y_6)\geq 0\wedge y_1\geq 0\wedge y_4\geq 0\wedge R_T>y_4\cot(y_6)\wedge R_T\tan(y_1)\leq r\tan(y_4)) \\
\vee(y_4\cot(y_6)\geq 0\wedge y_1>0\wedge y_4\geq 0\wedge R_T>y_4\cot(y_6)) \\
\left(\left|y_4\cot(y_6)\right|\geq 0\wedge y_1\geq 0\wedge y_4<0\wedge R_T>\left|y_4\cot(y_6)\right|\right)\vee \\
\vee\left(\left|y_4\cot(y_6)\right|\geq 0\wedge y_4<0\wedge R_T>\left|y_4\cot(y_6)\right|\wedge R_T\tan(y_1)\geq r\tan(y_4)\right)\vee \\
\vee\left(\left|y_4\cot(y_6)\right|\geq 0\wedge y_1>0\wedge y_4<0\wedge R_T>\left|y_4\cot(y_6)\right|\wedge R_T\tan(y_1)\geq r\tan(y_4)\right) \\
y_1=0\wedge y_4\geq 0\wedge R_T>\left|y_4\cot(y_6)\right|\wedge\left|y_4\cot(y_6)\right|>0\wedge R_T\tan(y_1)>r\tan(y_4) \\
\left(\left|y_4\cot(y_6)\right|\geq 0\wedge y_1<0\wedge R_T\tan(y_1)\geq r\tan(y_4)\wedge y_4\geq 0\wedge R_T>\left|y_4\cot(y_6)\right|\right) \\
\left(y_1=0\wedge y_4<0\wedge R_T>\left|y_4\cot(y_6)\right|\wedge\left|y_4\cot(y_6)\right|>0\wedge R_T\tan(y_1)\leq r\tan(y_4)\right)\vee \\
\vee\left(y_1\leq 0\wedge y_4<0\wedge R_T>\left|y_4\cot(y_6)\right|\wedge\left|y_4\cot(y_6)\right|>0\wedge R_T\tan(y_1)=r\tan(y_4)\right) \\
\left|y_4\cot(y_6)\right|\geq 0\wedge y_1<0\wedge R_T\tan(y_1)<r\tan(y_4)\wedge y_4<0\wedge R_T>\left|y_4\cot(y_6)\right|
\end{cases}
$$